

A STUDY OF RARE-EARTH DOPED SILICON-BASED FILMS AS A  
LUMINESCENT DOWNSHIFTING LAYER FOR CADMIUM TELLURIDE  
PHOTOVOLTAICS

A STUDY OF RARE-EARTH DOPED SILICON-BASED FILMS AS A  
LUMINESCENT DOWNSHIFTING LAYER FOR CADMIUM TELLURIDE  
PHOTOVOLTAICS

by

SNEHA BERNARD

B.Eng. & Society, McMaster University

A Thesis Submitted to the School of Graduate Studies in Partial Fulfilment of the  
Requirements for the degree Master of Applied Science

McMaster University

© Copyright Sneha Bernard, September 2014

Department of Engineering Physics

McMaster University Hamilton, Ontario

MASTER OF APPLIED SCIENCE (2014)

Title: A study of rare-earth doped silicon based films as a luminescent downshifting layer  
for cadmium telluride photovoltaics

AUTHOR: Sneha Bernard

SUPERVISOR: Dr. Peter Mascher

Number of pages: xvi, 88

## Contents

List of Figures .....	vii
List of Tables .....	xi
I. Abstract.....	xii
II. Contributions to the Field .....	xiv
a) Papers.....	xiv
b) Poster Presentations .....	xiv
c) Oral presentations .....	xiv
III. Acknowledgements.....	xv
IV. Introduction.....	1
a) Global Energy Trends .....	1
b) Photovoltaic Technology .....	3
i. Thin film photovoltaics .....	7
ii. Cadmium Telluride photovoltaics .....	10
c) Overview of Luminescent Downshifting (LDS).....	13
d) Photoluminescence from rare-earth ions.....	19
V. Materials and Methods .....	25
a) Sample Growth.....	25
i. Overview of PECVD .....	25

ii. Overview of annealing techniques .....	34
b) Characterization Techniques.....	36
i. Rutherford Backscattering Spectrometry .....	36
ii. Ellipsometry .....	39
iii. Transmission ellipsometry .....	43
iv. Photoluminescence.....	44
v. UV-Vis Absorption Spectroscopy .....	45
vi. Pulsed Laser Deposition of CdTe.....	47
VI. Results & Discussion .....	49
a) Rutherford Backscattering: Sample Composition.....	49
b) Photoluminescence .....	54
c) Ellipsometry .....	60
d) UV-Vis Absorption Spectroscopy .....	62
i. Absorption measurements .....	64
ii. Transmission ellipsometry .....	70
VII. Conclusions.....	75
a) Summary of Research Project.....	75
b) Improvements to Experimental Procedures .....	77
c) Suggestions for Future Work.....	78

d) Concluding Remarks.....	79
VIII. Appendices.....	81
Appendix A: Operation of MAC ECR PECVD system.....	81
IX. Works cited .....	85

## List of Figures

Figure 1: Global energy consumption patterns] Adapted from [1].....	1
Figure 2: Global energy consumption by fuel type. [1].....	2
Figure 3: GHG emission per kWh of electricity produced, by fuel type [2] .....	3
Figure 4: Schematic diagram of a p-n junction in a solar cell used to generate electricity [3].....	4
Figure 5: Charge separation at a p-n junction [3] .....	5
Figure 6: Shockley Queisser efficiency as a function of bandgap energy. Common photovoltaic material systems are also plotted, showing that most have a long way to go before reaching theoretical efficiency limits. [7] .....	6
Figure 7: Research cell efficiencies of different PV technologies, 1975-2012 [10].....	9
Figure 8: Schematic and cross sectional view of the superstrate configuration of a typical CdTe cell. [16] .....	11
Figure 9: Relative quantum efficiency curve of a CdTe cell from 200-1000nm [13] .....	12
Figure 10: AM 1.5G spectrum overlaid on the EQE curve of a high-efficiency CdTe cell. The high EQE region of the cell occurs between 500-750nm, suggesting that many higher energy photons between 200-300nm are wasted as they cannot be efficiently absorbed and used to generate EHPs by the cell. ....	13
Figure 11: Efficiency gap between theoretically calculated cell efficiencies and actual device efficiencies for various solar cell materials. [20] .....	15

Figure 12: Schematic drawing of an ideal LDS layer. In this ideal layer, it is assumed that all photons with energies above the bandgap are absorbed and emission only occurs at the bandgap energy. [22] .....	17
Figure 13: Orbital transitions and resulting emission wavelengths for rare earth elements [25] .....	20
Figure 14: Decomposition and surface reactions during the chemical vapour deposition process. [28] .....	25
Figure 15: PECVD chamber, depicting RF power source and magnetic field lines during the depositor process. [29] .....	26
Figure 16: Major sub-components of GIV ECR PECVD system in the Tandem Accelerator Lab at McMaster University [28] .....	28
Figure 17: Annealing furnaces with quartz tube holders. Furnaces were heated to 1200°C and ambient N <sub>2</sub> flowed over the samples during the annealing process. ....	35
Figure 18: Tandem Ion Beam at Tandetron Lab, Western University [30] .....	36
Figure 19: Ion-solid interactions [30] .....	37
Figure 20: Incident and backscattered ions during RBS, in the Cornell geometry. [30] .....	37
Figure 21: Linear, Circular and Elliptical polarization of the electric field vectors of propagating light waves. [32] .....	40
Figure 22 Incident and reflected beams during an ellipsometry measurement on a thin film sample [34] .....	41
Figure 23: Complete EASE ellipsometry model of Sample 006 annealed for 480 minutes. Note the low Mean Square Error of 8.04 using a Cauchy model. ....	43

Figure 24: Transmission ellipsometry experimental set up, showing 90° incident angle.....	44
Figure 25: Photoluminescence equipment set up at McMaster University, CEDT Labs. Aligned mirrors are used to direct a 325nm He-Cd laser towards a sample holder, and light is collected through an Ocean Optics spectrometer.....	45
Figure 26: Set up of absorption spectroscopy equipment [36] .....	46
Figure 27: Pulsed Laser Deposition chamber during CdTe growth [37].....	47
Figure 28: Representative RBS model of sample 005 .....	49
Figure 29: Cerium incorporation vs. cell temperature for previously grown samples. Similar data was not available for terbium incorporation. [25] .....	52
Figure 30: Rare earth incorporation vs. cell temperature for samples 000-008. There appears to be only a slightly discernible trend of higher incorporation with higher temperature. ....	53
Figure 31: PL results for Sample 003, annealed from 60-480 minutes, showing minimal emission at any wavelength, likely due to very low rare earth concentrations.....	56
Figure 32: PL results from sample 004, showing a broad, and likely non-rare earth related peak at certain anneal times, but minimal overall luminescence.....	57
Figure 33: PL results from sample 005, showing distinct rare-earth related peaks around 400nm (Ce) and 550nm (Tb) for all annealing times.....	57
Figure 34: PL intensities for all 480minute annealed samples, showing a consistent trend of increasing intensity with rare earth incorporation. ....	59
Figure 35: Refractive indices show a slight trend of increase with rare earth concentration for 480 minute annealed samples.....	62

Figure 36: Absorption measurements for films G007, CeORSO-27, and CeORSO-28 show similar trends in absorption profiles but much stronger absorption in samples with higher rare earth incorporation.....	65
Figure 37: LDS sample coupling with CdTe films. In the case of samples G007 and CeORSO 28 the samples were mounted on CdTe using optical cement. Sample CeORSO-27 was manually stacked on top of the CdTe film as there was very little of the sample left for future experiments. ....	66
Figure 38: Results of absorption measurements of CdTe coupled with sample G007, compared to that of sample G007 with no CdTe .....	67
Figure 39: Results of absorption measurements of CdTe coupled with sample CeORSO-28, compared to that of sample CeORSO-28 with no CdTe.....	68
Figure 40: Results of absorption measurements of CdTe coupled with sample CeORSO-27 mounted on CdTe, compared to that of sample CeORSO-27 with no CdTe.....	69
Figure 41: Transmission ellipsometry measurements- comparison between Samples G007, CeORSO-27 and Ce-ORSO-28 and their quartz and glass slide substrates .....	70
Figure 42: Results of transmission measurements of sample G007, compared to blank CdTe and the blank glass slide substrate .....	71
Figure 43: Results of transmission measurements of sample CeORSO-28, compared to blank CdTe and the blank quartz substrate .....	72
Figure 44: Results of transmission measurements of sample CeRORS-27, compared to blank CdTe and the blank quartz slide substrate.....	73

## List of Tables

Table 1: LCOE of different electricity generation technologies. Adapted from [8].....	8
Table 2: Growth parameters used to grow samples 000-005 on the MAC ECR PECVD system .....	31
Table 3: Growth parameters used to grow samples 006-008 on the GIV ECR PECVD system .....	32
Table 4: Growth parameters used to grow samples CeORSO-27 and 28 on the MAC ECR PECVD system .....	33
Table 5: Elemental composition of samples grown Note that the RE concentration of samples 000-004 is <0.1 at. %. Despite these essentially negligible concentrations, these samples were included in the data to illustrate general trends related to RE concentrations. ....	51

## I. Abstract

The peak efficiency range for CdTe solar cells is between 500-700nm; however efficiencies are limited at wavelengths shorter than 500nm due to the fact that at higher energies, most photons are absorbed in the CdS layer of the module and cannot contribute to the cell current. This means that incident photons with higher energies are ‘wasted’ as they are not efficiently absorbed by the cell. Luminescent downshifting (LDS) is a third-generation photovoltaic technology in which an external layer applied to the front surface of the cell absorbs high energy photons and re-emits them towards the cell at energies where they are more efficiently absorbed, thus avoiding front surface loss mechanisms.

This research project investigates the use of cerium and terbium co-doped silicon oxide thin films grown using electron cyclotron resonance plasma enhanced chemical vapour deposition (ECR PECVD) as a luminescent down-shifting layer. Post-deposition annealing in a quartz tube furnace caused the formation of cerium disilicate ( $\text{Ce}_2\text{Si}_2\text{O}_7$ ) nanocrystallites, which were found to strongly absorb incident light at wavelengths below 360 nm and efficiently sensitize  $\text{Tb}^{3+}$  ions in the film for re-emission. The effect of annealing time and sample composition on physical and optical properties was studied.

Film compositions were determined through Rutherford backscattering spectrometry, revealing an incremental increase in rare earth concentration. Photoluminescence measurements showed a distinct  $\text{Tb}^{3+}$  peak around 550nm, which is close to the ideal efficiency wavelength for CdTe photovoltaics. Variable Angle Spectroscopic Ellipsometry measurements were used to determine the index of refraction of as-deposited and annealed films. UV-Visible absorption spectroscopy and transmission

ellipsometry measurements showed a sharp increase in absorption around 400nm confirming wide separation between absorption and emission bands. When LDS films were coupled with thin film CdTe, subsequent absorption spectroscopy and transmission measurements showed stronger absorption at short wavelengths, as anticipated.

## II. Contributions to the Field

Various aspects of this research project have been presented at the following conferences and symposiums:

### a) Papers

**1) Society of Vacuum Coaters Tech Con (Chicago, IL, May 2014) Conference**

**Proceedings:** “A study of rare-earth doped silicon-based films as a luminescent downshifting layer for CdTe photovoltaic applications”

### b) Poster Presentations

**1) Nano Ontario (Kingston, ON, November 2013):** “A study of rare-earth doped

silicon-based films as a luminescent downshifting layer for CdTe photovoltaic applications”

**2) Materials Research Society Fall Meeting (Denver, CO, September 2013)** “A

study of rare-earth doped silicon-based films as a luminescent downshifting layer for CdTe photovoltaic applications”

### c) Oral presentations

**1) Society of Vacuum Coaters Tech Con (Chicago, IL, May 2014)** “A study of

rare-earth doped silicon-based films as a luminescent downshifting layer for CdTe photovoltaic applications”

**2) Functional Coatings and Surface Engineering Symposium (Montreal, QC,**

**June 2014)** “A study of rare-earth doped silicon-based films as a luminescent downshifting layer for CdTe photovoltaic applications”

### III. Acknowledgements

This thesis would not have been possible without the support of many people. First of all, I would like to thank my supervisor Dr. Peter Mascher for his guidance throughout this entire process, and for constantly encouraging me to attend conferences, meet with experts and develop my research and engineering skills. I sincerely appreciate the many opportunities and the constant enthusiasm and interest in my work.

Dr. Jacek Wojcik was an invaluable technical resource in growing and characterizing samples. Sincere thanks are due to him for always having the time and patience to explain difficult concepts, assist with growths and provide guidance on research topics. The CEDT staff and research engineers, were also always supportive and generous with advice.

Special thanks are also owed to past and present members of my research group- Patrick Wilson, Zahra Khatami, Owen Taggart and Austin Brown were all gracious enough to assist with experiments, discuss research and offer support whenever needed and I am sincerely grateful for their help. Many thanks also go to Dr. Preston and his research group for growing CdTe samples and assisting with subsequent characterization experiments. Dr. Lyudmila Gonchorova at UWO was an excellent resource for RBS characterization and I am extremely grateful for her help.

Without the generous financial support from NSERC CREATE and the Ontario Graduate Scholarship I would not have been able to pursue this degree or research project. Many thanks to all the administrative staff for their behind-the-scenes work in helping the past two years go so smoothly

Last but not least, I am forever thankful to my parents, and my partner Michael, for their unwavering support right from the very start of this degree. Thank you for your humour and encouragement when I needed it the most.

## IV. Introduction

### a) Global Energy Trends

Recent estimates from international energy agencies show that global energy demand is growing at an unprecedented rate. In 2010, global demand surpassed 500 quadrillion Btu, and a forecast for a demand of 820 quadrillion by 2040. As a result of rapid industrializing, most of the energy demand in the next few decades is anticipated to come from the developing world. The graph below shows the energy demand forecast for OECD and non-OECD nations (developed and non-developed nations) [1]:

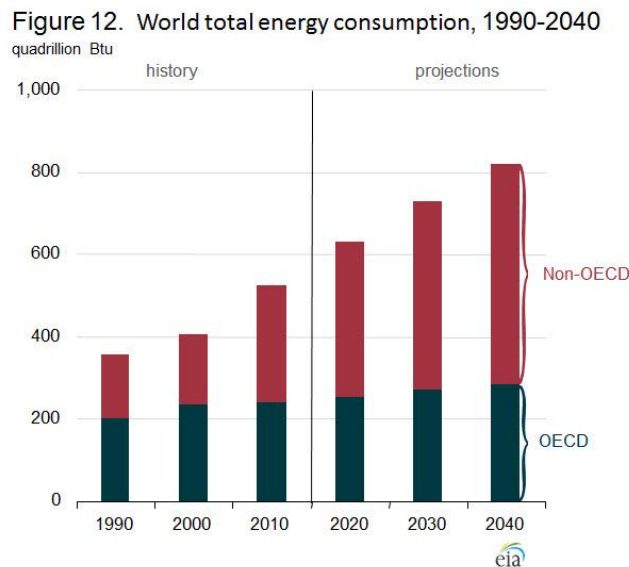


Figure 1: Global energy consumption patterns] Adapted from [1]

While access to energy and electricity signals an improvement in quality of life for a large portion of the world's population, the reality is that increased energy consumption traditionally leads to an increase in greenhouse gas emissions. As shown in

the graph below, fossil fuels are projected to play a significant role in meeting this dramatic increase in energy consumption [1]. Figure 2 shows that despite a promising increase in renewable sources, fossil fuels will continue to dominate the global energy landscape in the foreseeable future.

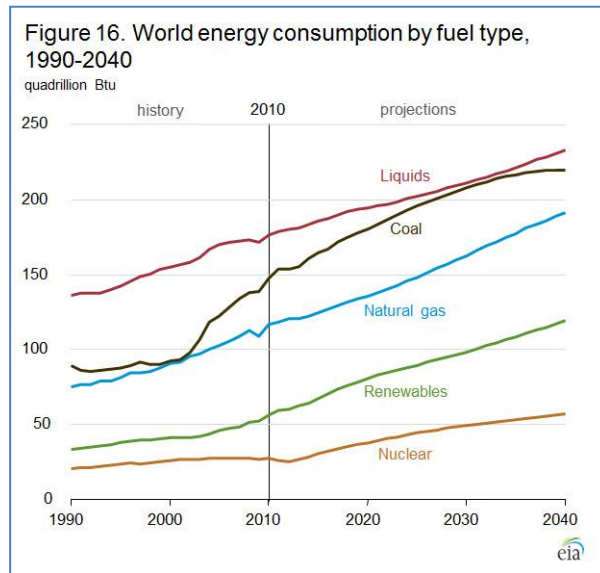


Figure 2: Global energy consumption by fuel type. [1]

A lifecycle analysis of various fuel types places solar photovoltaic technology amongst the lowest greenhouse gas emitters per kWh of electricity produced (typically estimated to be around 30g CO<sub>2</sub>e/kWh for most mainstream PV technologies), as shown in Fig. 3. With increasing awareness about the detrimental impacts of climate change, photovoltaic technology is rapidly emerging as an elegant solution to an imminent global energy crisis.

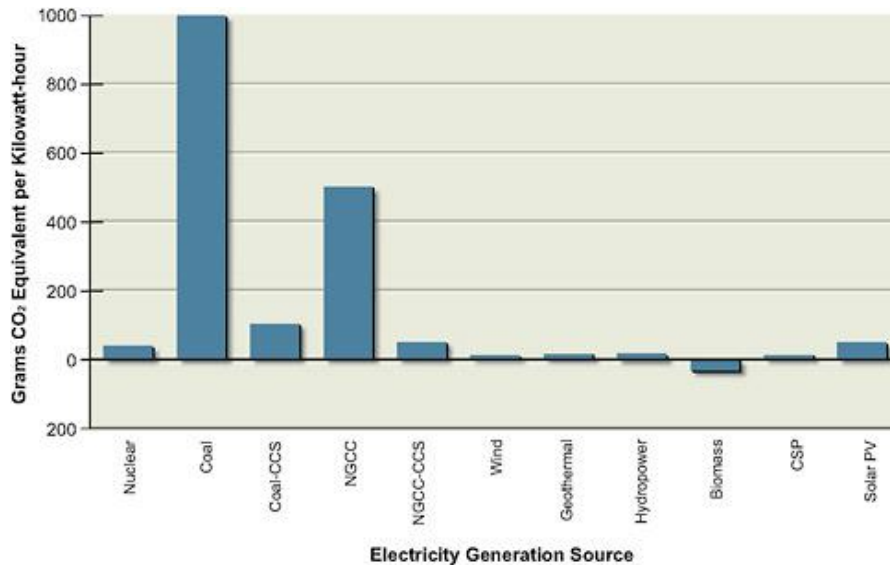


Figure 3: GHG emission per kWh of electricity produced, by fuel type [2]

In 2012, there was 96.5 GW of installed photovoltaics globally, with some sources suggesting that undocumented installations in the developing world push this number over 100 GW. However despite promising growth, photovoltaics account for only a small percentage of electricity production in most nations. This low percentage can be largely attributed to the fact that despite low infrastructure requirements, PV technology remains one of the more expensive forms of electricity generation. Education, as well as improvements in manufacturing and technical advances in efficiency will do much to increase PV's proportion of the energy market in the upcoming years.

## b) Photovoltaic Technology

A simple schematic diagram of a single junction solar cell is shown below:

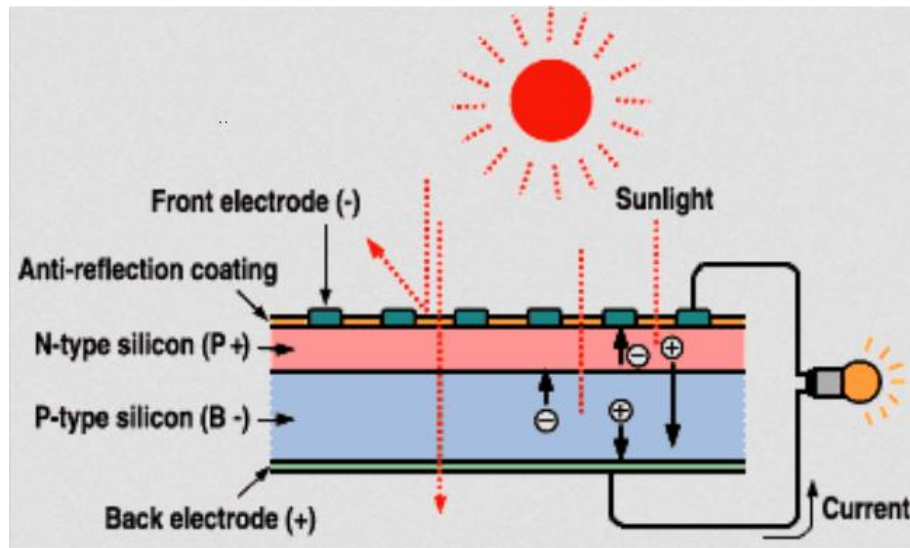


Figure 4: Schematic diagram of a p-n junction in a solar cell used to generate electricity [3]

Photovoltaic technology operates on three basic processes [4]:

- Absorption of photons: When a photon with energy greater than the bandgap (difference in energy states between the conduction and valence bands of the material) is incident upon the solar cell, it can be absorbed. The photon energy creates an electron hole pair (EHP) by promoting an electron from the valence to the conduction band.
- Separation of charge carriers: The depletion region at the p-n junction of the solar cell creates an electric field that “pushes” the charged carriers away from the junction towards the respective p and n regions of the solar cells, thus causing dissociation of the EHPs.
- Transportation of charge carriers to external contacts where they generate a cell current: If connected via a conducting material, this dissociation of carriers causes a current flow across oppositely charged ends of the junction,

producing a cell current and voltage, to attempt to “equalize” the potential difference.

This process is depicted schematically in Fig 5 below:

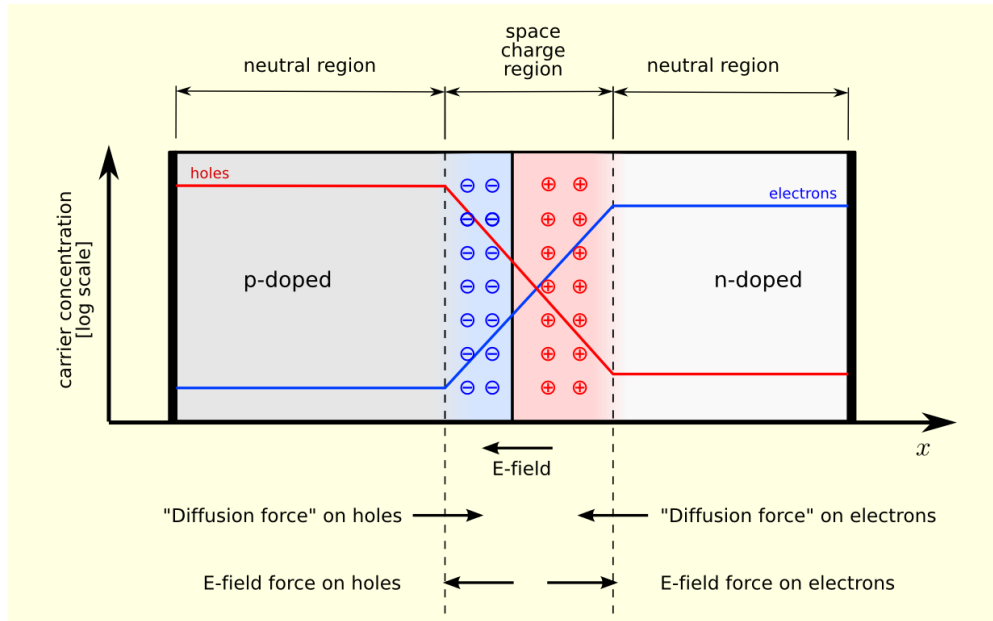


Figure 5: Charge separation at a p-n junction [3]

The diode equation dictates that the current of a solar cell under illumination is a function of the generated current and the dark cell current. This is given by the equation:

$$J = J_L - J_0 \left( \exp \left[ \frac{qV_{OC}}{nkT} \right] - 1 \right)$$

where  $J_L$  is the generated current and  $J_0$  is the reverse saturation current (dark current). Conversely, this equation can be used to determine the open circuit voltage,  $V_{OC}$ , defined as the maximum voltage, occurring when the net current flow is 0. [5]

The Shockley-Queisser limit, derived in 1961 by William Shockley and Hans Queisser, calculates the maximum efficiency possible in a single junction solar cell as a function of the bandgap energy. [6] This limit, also known as the detailed balance limit is calculated based on several key assumptions:

- The solar spectrum is based on blackbody radiation from the sun at a temperature of 6000K
- Only photons with an energy  $h\nu > E_g$  will be absorbed by the semiconductor material
- Each absorbed photon will create a single EHP, and the major loss mechanism is radiative recombination.

The Shockley Queisser limit is plotted against bandgap energy in Fig. 6 below, along with the bandgap and efficiencies of common photovoltaic materials.

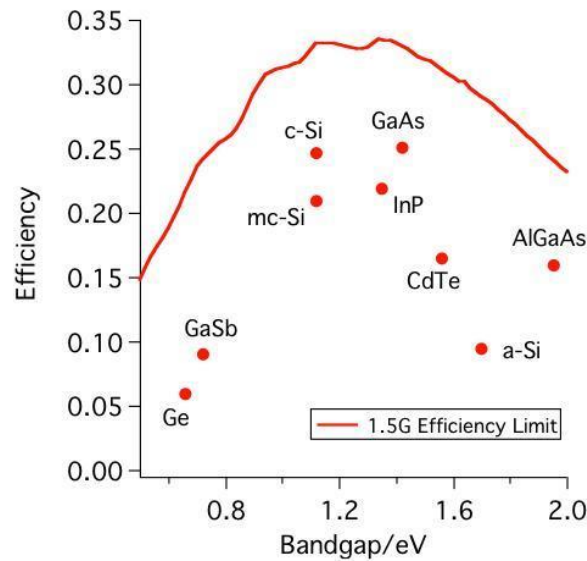


Figure 6: Shockley Queisser efficiency as a function of bandgap energy. Common photovoltaic material systems are also plotted, showing that most have a long way to go before reaching theoretical efficiency limits. [7]

From this graph CdTe appears to be uniquely positioned with a close to ideal bandgap of 1.5eV (the peak efficiency occurs at 1.4eV) but a lower than average efficiency. Thus, there is significant room for improvement before CdTe photovoltaics reach their Shockley Queisser limit. However, in most solar cells, there are much more stringent limiting factors than those imposed by the Shockley Queisser limit. These include reflection losses (somewhat mitigated by the application of anti-reflective coatings) and EHP recombination losses due to defects, traps and grain boundaries.

#### **i. Thin film photovoltaics**

A major obstacle to the widespread adoption of PV is the prohibitively high cost. The Levelized Unit Cost of Energy (LCOE) is a common metric used to compare the costs of different forms of electricity production, throughout their life cycles. In its annual energy outlook report, the US Department of Energy predicted that despite advances in manufacturing and installation technology, the cost of solar photovoltaics technology would remain higher than traditional electricity generation technologies. This is shown in Table 1 below:

<b>Plant type</b>	<b>Capacity factor (%)</b>	<b>Total system levelized cost</b>
<b>Dispatchable Technologies</b>		
Conventional Coal	85	100.1
Advanced Coal with CCS	85	135.5
Natural Gas: Conventional Combined Cycle	87	67.1
Advanced Nuclear	90	108.4
Geothermal	92	89.6
Biomass	83	111

<b>Non-Dispatchable Technologies</b>		
Wind	34	86.6
Solar PV <sup>1</sup>	25	144.3
Solar Thermal	20	261.5
Hydro	52	90.3

**Table 1: LCOE of different electricity generation technologies. Adapted from [8]**

Since they use less material, thin film photovoltaics are able to dramatically reduce the cost of PV technology. There is a wide range of thin film PV technologies, ranging from Group III-V materials (GaAs, etc), CdTe and CIGS technology to amorphous silicon solar cells. Thin film PV modules can range in thickness from several nanometers to a few microns thick, and are commonly used in Building Integrated PV applications and handheld electronics and are rapidly gaining popularity in the mainstream commercial PV market place. [9] The infographic below from NREL (Fig 7.) shows that despite lagging behind other technologies initially, thin film PV has made huge strides in efficiency.

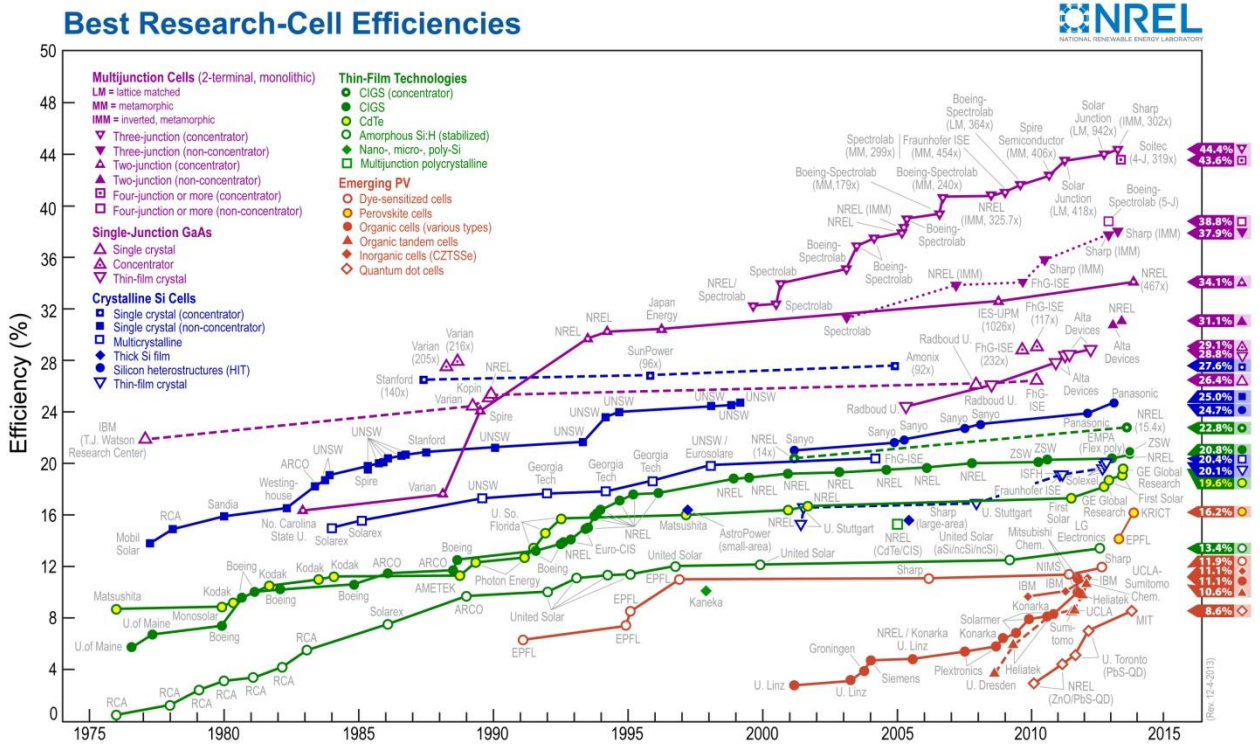


Figure 7: Research cell efficiencies of different PV technologies, 1975-2012 [10]

Due to cheap, flexible substrates and innovative deposition techniques thin film photovoltaic technologies are a huge factor in reducing solar energy costs. Market research shows that thin film technology (primarily CIGS and amorphous Si) accounted for almost 25% of the solar market share in 2009. As material availability, ecological impact and an urgent need for renewable energy become a pressing public concern, it is very likely that thin film technology will play a prominent role in meeting global energy needs. [11]

## ii. Cadmium Telluride photovoltaics

Due to their potential for high efficiency and long term stability, CdTe thin film photovoltaic technology is rapidly gaining a large share of the global photovoltaic market. Crystalline CdTe was first grown by vapour deposition in 1947, and its optical properties and electronic characteristics were subsequently characterised, forming the basis for modern CdTe technology. An initial attempt to develop this material into photovoltaic devices in the 1950's resulted in cells with relatively low conversion efficiencies and poor crystal quality. [12] In the early days of CdTe technology, concerns were raised about the high toxicity of cadmium when released into the environment; however the implementation of rigorous recycling programs in recent years has ensured that almost all cadmium from defunct solar panels can be recovered and re-processed into new devices. [13]

CdTe is a popular material choice for thin film solar cells: it has a direct bandgap of 1.5eV, a high absorption coefficient of  $6 \times 10^4/\text{cm}$  (at 600nm), and it is a good spectral match for our sun. [14] Today, thin film CdTe photovoltaic technology has achieved conversion efficiencies of close to 20% [15], using a superstrate configuration, in which CdTe is deposited on a transparent substrate such as glass or sapphire, followed by the deposition of the CdS window layer and a transparent conducting oxide (TCO) layer. The most common fabrication techniques for this structure include electro-deposition, closed-space sublimation, physical vapour deposition, and sputter deposition, followed by a post deposition treatments with  $\text{CdCl}_2$  and  $\text{O}_2$  to remove native defects and obtain the desired electronic structure of the CdTe and CdS layers. Additionally, these

post-deposition treatments are used to increase grain size and reduce losses associated with grain boundaries. The development of low resistance contacts has also contributed significantly to efficiency increases in recent years. [12] Figure 8 below shows a cross sectional view of the superstrate configuration [16]:

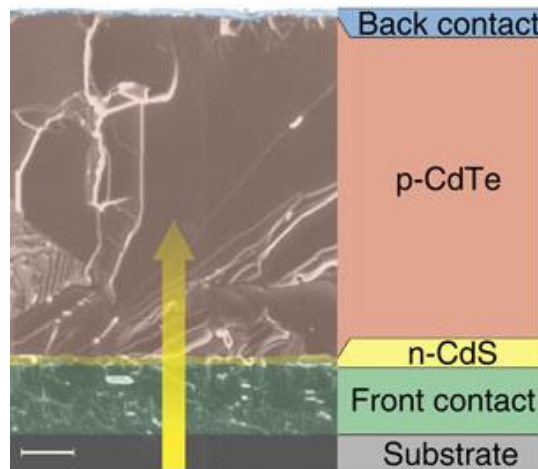


Figure 8: Schematic and cross sectional view of the superstrate configuration of a typical CdTe cell. [16]

In this configuration, light enters the cell through the transparent substrate, and charge separation occurs at the CdTe/CdS heterojunction. Ensuring a thin CdS layer helps to minimize the number of photons with energy above the CdTe bandgap that are absorbed in this layer, but this also reduces the maximum photocurrent. Techniques to address this issue currently involve mixing CdS with ZnS to further increase the bandgap and thereby the transmission of photons; however, this shows limited efficiency improvements. Additionally, very thin CdS layers contribute to excessive forward current and local shunting, further diminishing cell current.

This effect can be better explained by observing the external quantum efficiency (EQE) curve for a 16.4% efficient CdTe cell developed by a team at NREL, shown in Fig. 9 [17]:

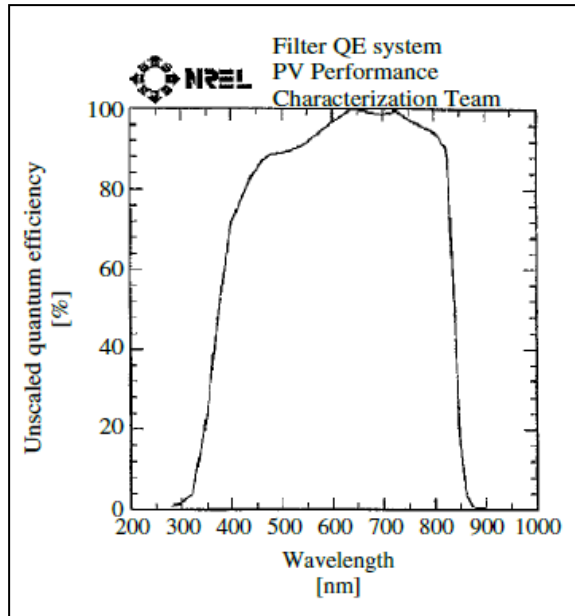
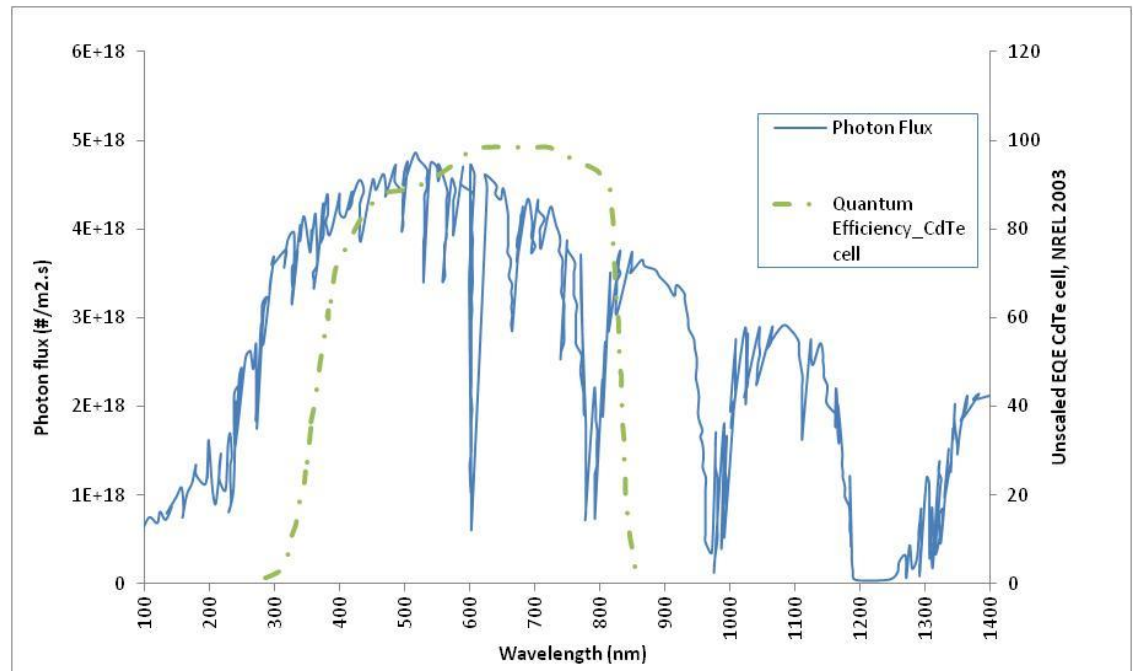


Figure 9: Relative quantum efficiency curve of a CdTe cell from 200-1000nm [13]

Fig. 10 below shows the quantum efficiency curve from Fig. 9 overlaid on the AM 1.5 G photon flux spectrum.



**Figure 10: AM 1.5G spectrum overlaid on the QE curve of a high-efficiency CdTe cell. The high EQE region of the cell occurs between 500-750nm, suggesting that many higher energy photons between 200-300nm are wasted as they cannot be efficiently absorbed and used to generate EHPs by the cell.**

The data shows that a significant portion of the photon flux incident on a CdTe cell falls outside the peak efficiency range of 500-800nm. If the short wavelength, high energy photons could be absorbed and ‘shifted’ (i.e. re-emitted) to longer wavelengths before entering the cell, they would be absorbed by the CdTe layer rather than the high bandgap CdS. This shift to wavelengths where the cell performs more efficiently is the goal of luminescent downshifting that will be addressed in this thesis.

### **c) Overview of Luminescent Downshifting (LDS)**

Spectral modification is a common technique to improve the efficiency of third-generation photovoltaics. It is accomplished by one of three techniques listed below [18]:

- i. Up-conversion: two low-energy photons are combined to produce one high energy photon
- ii. Down conversion: one high-energy photon is ‘cut’ to produce two low energy photons
- iii. Luminescent down-shifting (LDS): High energy photons lose some energy and shift into a more favourable spectral range for the solar cell.

Spectral losses, arising from an inability of the solar cell in question to properly absorb a photon of a specific wavelength and generate a photocurrent, are a significant proportion of losses in photovoltaic technologies, including thin film cells. The Shockley-Queisser limit for a single junction CdTe cell places the maximum theoretical efficiency at approximately 31% while most commercially available modules have efficiencies around 15%. [19] The performance gap between the theoretical efficiencies and the maximum achieved cell efficiencies to date is shown below. Spectral losses account for some of the discrepancy in each case as do thermalization losses, recombination losses and other material and device parameters. [20]:

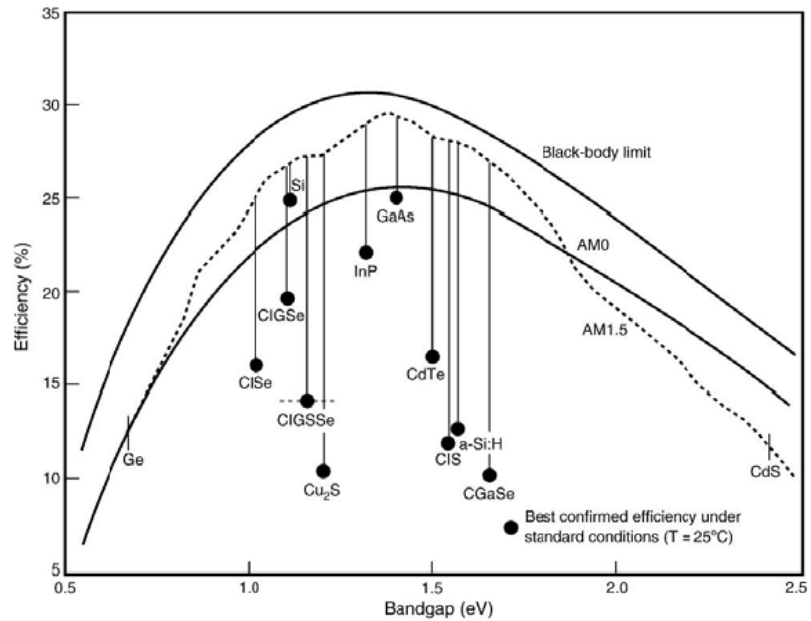


Figure 11: Efficiency gap between theoretically calculated cell efficiencies and actual device efficiencies for various solar cell materials. [20]

Spectral losses are due to both the transparency of the material for photons with energies below the bandgap; as well as to radiative recombination losses from the absorption of photons with energies above the bandgap. High energy photons tend to be absorbed near the surface of the cell, where recombination rates are highest. [18] These losses can be mitigated by modifying the cell to better utilize the short wavelength range of the spectrum; however many modifications are expensive to implement in commercial processing facilities. In CdTe/CdS photovoltaic modules, the CdS window layer, with a bandgap of 2.4eV preferentially absorbs high energy photons before they can be usefully absorbed by the CdTe layer. Traditional approaches to this problem (as discussed previously) have involved thinning this layer to minimize absorption, with limited commercial success.

Luminescent downshifting layers provide an attractive alternative to this problem- they absorb photons at short wavelengths and re-emit them at longer (more favourable) wavelengths thus modifying the spectrum incident on the cell. By shifting high energy photons to lower energies, the losses of electron-hole pairs due to various recombination processes can be reduced, thus improving performance at these higher energies. It is important to note that since the LDS layers are electronically decoupled from the cell, they do not affect the open circuit voltage ( $V_{oc}$ ) or other electronic properties. Furthermore, unlike up-conversion and down-conversion they do not push efficiencies past the SQ limit for a single junction, but instead help to mitigate losses that prevent current technology from achieving the SQ limit [18]. The implementation of these layers also removes many constraints of the design of the underlying photovoltaic cell itself, and can generally be applied easily and cost-effectively in a commercial environment. [21] A schematic diagram of an LDS layer is shown below:

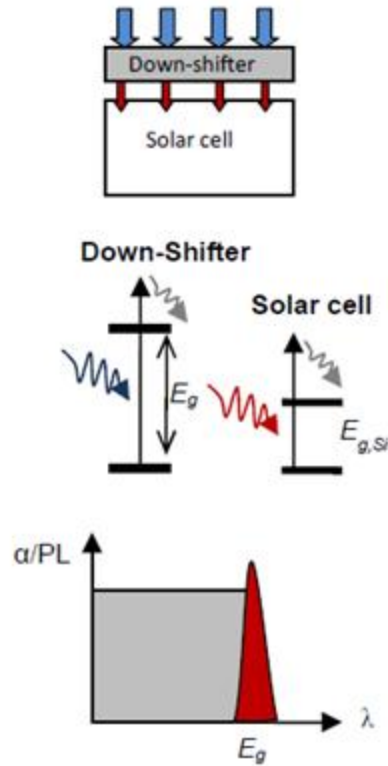


Figure 12: Schematic drawing of an ideal LDS layer. In this ideal layer, it is assumed that all photons with energies above the bandgap are absorbed and emission only occurs at the bandgap energy. [22]

Work in this field began in the 1970s, when researchers demonstrated significant improvements in efficiency resulting from LDS layers in GaAs and CuS/CdS cells. [23] Today, LDS systems are composed of luminescent dyes in organic polymer host matrices, quantum dots in semiconductor matrices, and rare earth doped semiconductor films. It is important to note that any further interfaces that incident light needs to pass through to reach the cell will invariably introduce new sources of losses, so several factors need to be considered in the design of an LDS system. The most significant loss mechanisms are listed below [21]:

- i. Emission at less than unity from the LDS layer (i.e. not all absorbed photons are re-emitted to the cell)
- ii. Photons not emitted in the direction of the cell are lost from the LDS layer
- iii. Re-absorption of photons by the layer due to overlapping absorption and emission bands.
- iv. Reflection from the two interfaces of the layer
- v. Parasitic absorption from the host material of the LDS layer.
- vi. Absorption in regions of the spectrum that should not be downshifted (ideally, the LDS layer would be transparent to all wavelengths that do not need to be downshifted).

Additionally, different treatment mechanisms during the deposition of the LDS layer may affect the material properties of the photovoltaic cell, so it is important to choose compatible material systems. In order to justify the application of the layer, these losses must be compensated by a higher gain in efficiency of the cell. Past research shows that internal quantum efficiencies of up to 50-60% have been achieved and up to 75% of photons can be directed toward the solar cell. [22] In order to justify the increase in manufacturing costs, the efficiency improvements must be significant so that the total cost per unit power produced for the modules decreases or remains constant. Current research suggests that the spectral response of CdTe/CdS modules makes them a promising candidate for LDS layers, and efficiency increases of up to 40% are theoretically achievable. [21] The most common LDS material choices for CdTe/CdS cells to date have been organic dyes and polymers, however; little research (if any) has

been conducted towards the application of rare earth ion systems in semiconductor host matrices.

#### **d) Photoluminescence from rare-earth ions**

Despite their name, rare-earth elements are a ubiquitous family of elements relegated to the lanthanide family in the periodic table (ranging from lanthanum to ytterbium). However, despite their general plentitude they are typically found in low concentration deposits throughout the earth's crust, thus giving rise to the name "rare-earth." Rare earth elements are currently widely used in magnets, optoelectronic devices (most commonly the Nd-YAG laser), catalysts, lighting applications and green energy technologies. The light emitting properties of lanthanide elements have also been widely studied and exploited in many phosphorescent screen technologies for much of the 20<sup>th</sup> century.

The lanthanide elements are known for their partially filled 4f electronic orbital, shielded by the (filled) 5s<sup>2</sup> and 5p<sup>6</sup> orbitals rendering them insensitive to the host matrix material and structure. When used to dope crystalline silicon, III-V semiconductors or other optoelectronic materials, the rare earth elements are incorporated in ion form. Specifically, terbium and cerium which were the elements used in this research project are incorporated into the silicon oxide host matrix in the 3+ forms. [24]

In the optoelectronics sector, rare earth ions are valued for their unique photoluminescent properties, namely high intensity and narrow line width. Upon absorbing a photon, and transferring energy to the electrons, the narrow line of emission



These transitions are parity forbidden, which means that electronic transitions between like orbitals (f to f, d to d, etc.) are forbidden. However, due to the weak interactions of the ion with the surrounding crystal field, mixing of opposite parity wave function occurs and the transition is allowed. The exception to this rule is the  $\text{Ce}^{3+}$  transition which occurs between the 5d and 4f levels, which is not parity forbidden and thus has a broader linewidth. [25]

When incorporated into a solid host matrix (such as the silicon oxide films used in this experiment) the ions tend to precipitate in the form of aggregates or compounds with elements in the host matrix. In the cerium and terbium co-doped films, the cerium reacts with the silicon and oxygen in the sample to form cerium disilicate ( $\text{Ce}_2\text{Si}_2\text{O}_7$ ) while the terbium remains suspended in the host matrix in aggregate form. Rare earth solubility in host matrices imposes an upper limit on how much can be incorporated into a film: at high concentrations, the formation of large aggregates of rare earth ions causes quenching of luminescence due to ion-ion interactions, in which energy transfer between rare earth species causes non-radiative decay. [24]

There can be several radiative energy transfer mechanisms involved between rare-earth ions, however since this experiment relies on energy transfer from nanostructures in the films to the terbium ions, the mechanisms are slightly different. Upon annealing at high temperatures, the cerium ions incorporated into the films amalgamate into crystalline nanostructures within the amorphous host matrix. Heisenberg's uncertainty principle explains that as the uncertainty in the position of an electron decreases, the uncertainty in its momentum (and thereby energy) increases as per the equation:

$$\Delta x \Delta p \geq \frac{\hbar}{2}$$

Thus, as the uncertainty of the position of the electrons decreases due to the nanoscale size of these features, the uncertainty in its energy increases and upon excitation, the electron is able to achieve a quasi-direct transition from an excited to a relaxed state, via emission of a photon. By altering the physical dimensions of the nanocrystals, it is thus possible to tune the bandgap of the material via this quantum confinement effect, unlike that of a bulk structure. [25] This is, in essence, the mechanism used to achieve luminescence from silicon nanocrystals. For a thorough examination of the quantum confinement effect and its application in silicon nanostructures please refer to [4].

The effect of adding cerium into the nanostructures was manifold: firstly due to the clustering effect of cerium, solubility limitations associated with incorporating bulk silicon were largely overcome. (The solubility limitation refers to the effect of precipitation of the rare earth ions into alloys with the host material, at high concentrations, which leads to quenching of luminescence.) Secondly, the presence of cerium affects the absorption spectra of the nanostructures, causing strong absorption at blue-UV wavelengths (which is ideal for CdTe photovoltaics which exhibit low EQE in this region). Finally, rather than emit at the bandgap of the cerium disilicate nanostructures (350-450nm), the energy emitted excites the  $Tb^{3+}$  ions still present in the host matrix, which in turn emit across the intra 4f energy bands, as described previously. [25]

This secondary excitation process is known as Förster-Dexter coupling, in which electronically forbidden transitions are allowed due to the overlapping dipole electric field of the sensitizing and activated ions (Ce and Tb respectively), via emission of a virtual photon. This process is known as sensitized luminescence, and specifically refers to the phenomenon in which a dopant atom is made to emit via energy transfer from another dopant atom. The efficiency of process is inversely proportional to the distance between the two systems, and thus efficiency increases with increased concentration of the sensitizing and activated ions, as their dipole fields are statistically more likely to overlap. The increased formation of nanocrystals in the host matrix also contributes to increased luminescence efficiency as there are more sensitizers available to activate the Tb ions. [26]

Typically rare earths have been employed in the development of up-converting materials- erbium and ytterbium have both been used to combine low energy photons through similar radiative processes as described above, to produce high energy photons that are absorbed in high EQE regions of the solar cells. In the past, luminescent downshifting efforts have focused primarily on the use of cheap and abundant polymers and dyes. However, as rare earth emissions are increasingly well researched and documented, rare earth based LDS have seen increased investment in R&D efforts, due to their long term stability and narrow emission linewidth. Recently, terbium and europium have been used to demonstrate downshifting from UV to red wavelengths, when incorporated into an organic polymer host matrix. [27] As novel fabrication techniques

develop, and absorption and quantum yields improve, there is likely to be much more research conducted into the role of rare-earth elements in third generation photovoltaics.

## V. Materials and Methods

### a) Sample Growth

#### i. Overview of PECVD

Chemical vapour deposition is a thin film growth technique in which precursor gases introduced into a vacuum chamber decompose and react on a solid substrate to form a thin film layer. Precursor molecules impinge on the substrate surface as shown schematically in Fig. 14 (using the example of  $\text{SiH}_4$  and  $\text{O}_2$  precursor gases), and if the substrate is heated to a temperature that provides sufficient thermal energy, they will decompose to form a thin film (in this case  $\text{SiO}_2$ ).

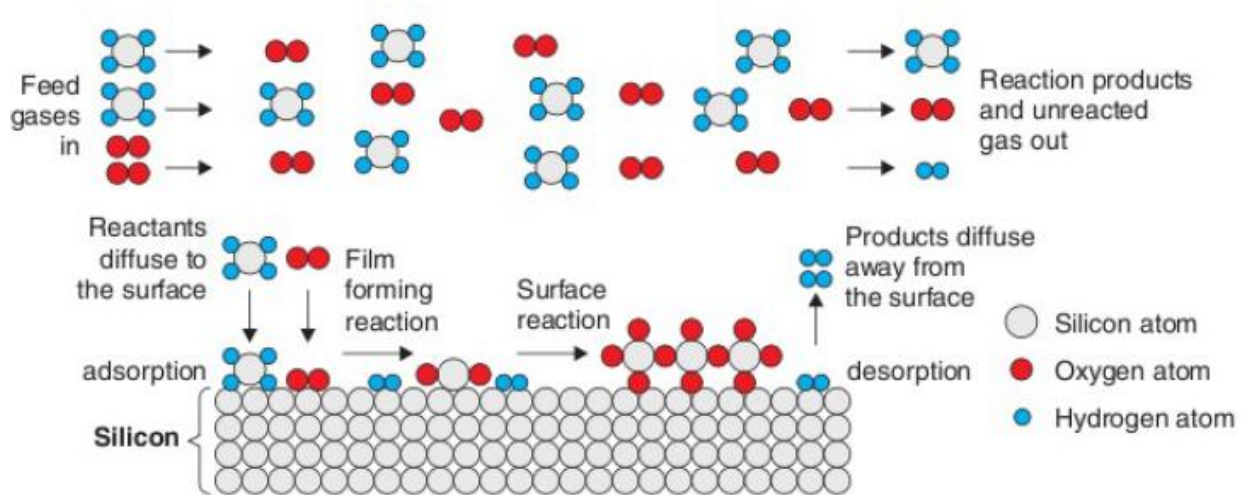


Figure 14: Decomposition and surface reactions during the chemical vapour deposition process. [28]

Reactive by-products are then removed from the deposition chamber and exhausted in a safe manner to remove toxic gases. Plasma Enhanced Chemical Vapor

Deposition (PECVD) is a CVD technique that uses plasma to lower the thermal energy threshold for thin film growth, so that films can grow at relatively lower temperatures. A plasma is an ionized gas found in very high temperature systems that provide sufficient energy for the gas molecules to exceed their ionization energies. In the PECVD system used in these experiments, a plasma was generated through a process known as electron cyclotron resonance. In this process, radio frequency (RF) power is applied to ions in a vacuum container that has a magnetic field applied across it. The generated plasma is extracted from the chamber and a constant influx of atoms is maintained to ensure a constant plasma density [28]. This process is depicted schematically in Fig. 15 below:

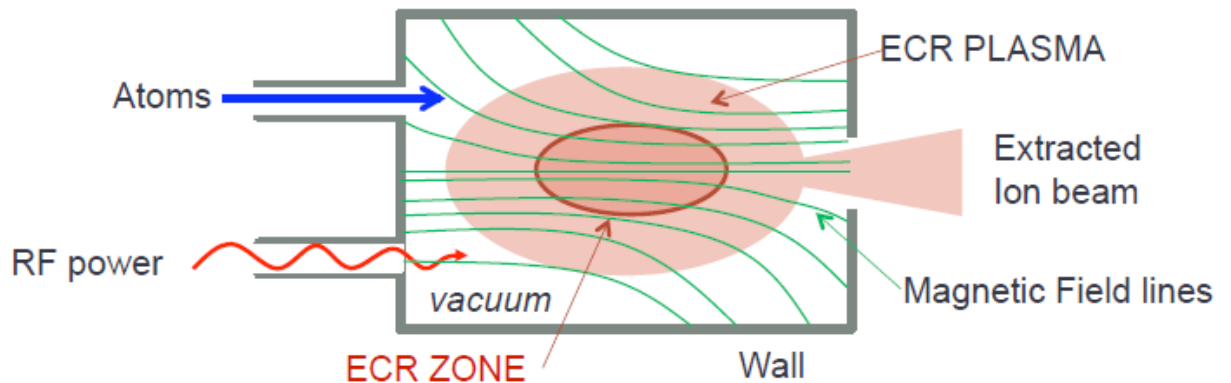


Figure 15: PECVD chamber, depicting RF power source and magnetic field lines during the depositor process. [29]

The rate of reaction on the substrate depends on several factors including the atomic flux on its surface. The atomic flux (atoms/m<sup>2</sup>-second) incident on the substrate surface can be described by the equation [28]:

$$J = \frac{nc_{mean}}{4}$$

In this equation,  $c_{mean}$  is the mean speed of the atoms in an ideal gas, given by Maxwell's equations and the  $\frac{1}{4}$  factor is derived by assuming that half the ions are moving away from the substrate surface, while another quarter are moving parallel to it.

The rate of reaction R is given (nm/minute) by the equation:

$$R = \frac{K_{surface}n}{\rho_m}$$

where  $K_{surface}$  is the probability of a reaction occurring on the surface, n is the species concentration and  $\rho_m$  is the film's molar density.

The ECR PECVD system used to grow the films in this research project is shown in Fig. 16, with each of its major sub-components.

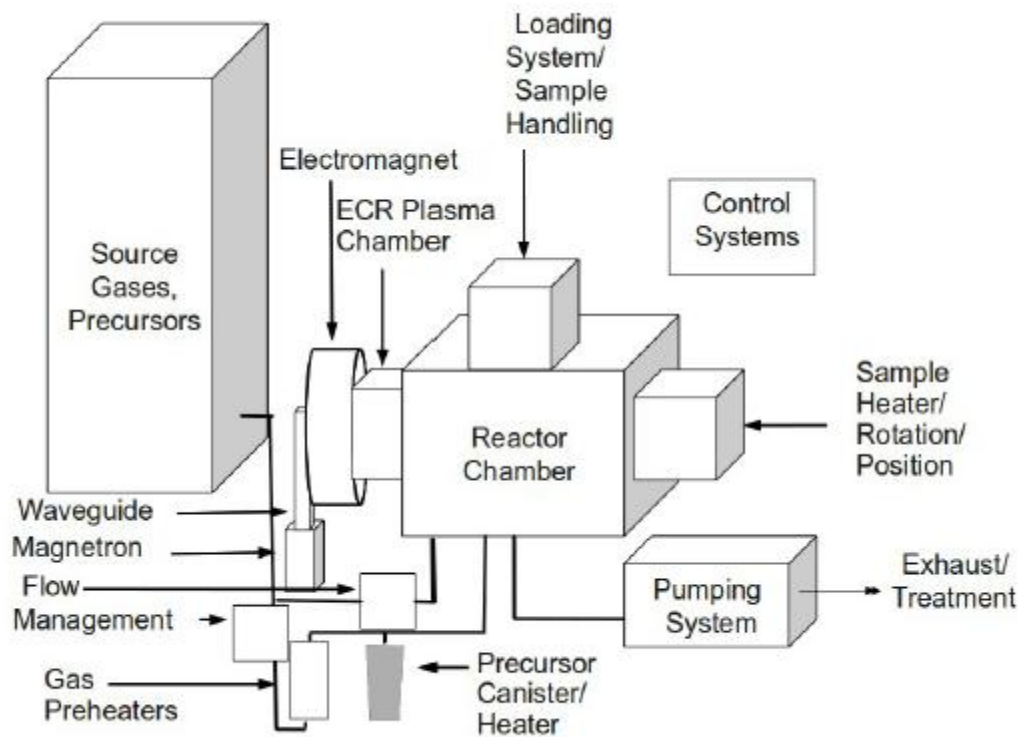


Figure 16: Major sub-components of GIV ECR PECVD system in the Tandem Accelerator Lab at McMaster University [28]

The magnetic field is generated by the large circular electromagnet supplied with a current of 180A and water cooled using chilled water pipes that wrap around the subsystem. The microwave source consists of a microwave power supply that supplies a magnetron with an output of 200-1000W. During this experiment, magnet power was held constant at 500W, and a reflected power detector was used to ensure that  $P_{incident} - P_{reflected} = 500W$  throughout the deposition process. The reactor chamber pressure was maintained using a series of high vacuum and ultra high vacuum pumps, monitored using a series of ion gauges. Typical base pressures were maintained at  $10^{-6}$  Torr.

The sample was loaded into the deposition chamber through a load lock system. While loading and unloading the sample, the load lock chamber is vented with nitrogen to reduce the chance of moisture entering the deposition chamber which could damage the ultra high vacuum system. Once the sample is loaded, the load lock chamber is pumped down to a low pressure before opening the main gate to insert the sample into the deposition chamber followed by subsequent pumping to ultra high vacuum pressures (on the order of  $10^{-9}$  Torr)

Gas flows were delivered to the deposition chamber via a series of gas flow valves opened during the deposition process. Silane, argon and oxygen flows were delivered to form the oxygen rich silicon oxide film, while external rare earth cells were heated and cerium and terbium ions delivered to the reaction chamber via an argon gas flow. All gas flows were calibrated using mass flow controllers, calibrated for each specific gas and delivered from external cylinders. Gas flows used to grow samples are shown in Table 2, 3 and 4.

Once the silane reaches the chamber a consistent dispersion is needed to create a uniform thin film layer, which is achieved using a “shower head” configuration to release the gas into the chamber. Other gases (nitrogen, argon, oxygen) were delivered through outlets in the deposition chamber. In order to deliver the rare earth atoms into the chamber, the canisters held in an external cell were heated to the desired temperature (see Results and Discussion section for cell temperatures and sample composition) and the accompanying lines and rings used to deliver it into the chamber were also heated to ensure that the heated gases did not re-condense and block the lines. The sample stage

was heated up to a temperature of 100°C in order to maintain a substrate temperature conducive for the reaction of precursor gases and the formation of a thin film layer. A step by step procedure of the set up and deposition process is provided in Appendix A.

The goal of sample growth in this research project was to produce a series of oxygen rich silicon oxide films with increasing rare earth concentration, at consistent thicknesses of 1000-2000Å. The silicon and oxygen concentrations were kept relatively constant at approximately 35% and 65% respectively, while a maximum of 5% cerium and 1% terbium was to be incorporated into the films. A summary of growth parameters and conditions are shown in Table 2, 3, and 4 below. Samples in Table 2 were grown on the MAC ECR system, while samples in Table 3 were grown using the GIV ECR system. The final set of samples in Table 4 were grown several months prior to this research project, on the MAC ECR system. .

Table 2: Growth parameters used to grow samples 000-005 on the MAC ECR PECVD system

	Sample	Substrate	Gas flow rates (sccm)			Deposition pressures ( $\pm 0.1$ mTorr)	Temperatures ( $^{\circ}\text{C}$ )				Power (W)		Deposition time (min)
			SiH <sub>4</sub> / Ar	O <sub>2</sub> /Ar	RE/Ar		Tb	Ce	RE lines and ring	Stage heater	Discharge	Reflected	
Mac ECR	000	n type (100) Silicon	2	19	0	1.5	0	0	225	100	500	0	20
	001	n type (100) Silicon	2	19	5	1.9	120	170	225	100	500	0	25
	002	n type (100) Silicon	2	19	5	1.6	125	180	225	100	500	0	15
	003	n type (100) Silicon	2	19	5	2.3	130	180	225	100	500	0	25
	004	n type (100) Silicon	2	19	5	2.3	135	180	225	100	500	0	25
	005	n type (100) Silicon	2	19	5	2.3	140	180	225	100	500	0	25

Table 3: Growth parameters used to grow samples 006-008 on the GIV ECR PECVD system

			Gas flow rates (sccm)			Deposition pressures ( $\pm 0.1$ mTorr)	Temperatures ( $^{\circ}\text{C}$ )				Power (W)		Deposition time (min)
			Sample	Substrate	SiH <sub>4</sub> / Ar		O <sub>2</sub> /Ar	RE/Ar	Tb	Ce	RE lines and ring	Stage heater	Discharge
GIV ECR	006	n type (100) Silicon	2	20	5	3.2	133	180	225	100	503	3	60
	007, G007	n type (100) Silicon, glass slide	2.5	25	5	3.8	181	219	225	100	503	3	90
	008, G008	n type (100) Silicon, glass slide	2.5	25	5	3.8	200	217	225	100	503	3	90

**Table 4: Growth parameters used to grow samples CeORSO-27 and 28 on the MAC ECR PECVD system**

	Sample	Substrate	Gas flow rates (sccm)			Deposition pressures ( $\pm 0.1$ mTorr)	Temperatures ( $^{\circ}\text{C}$ )				Power (W)		Deposition time (min)
			SiH <sub>4</sub> / Ar	O <sub>2</sub> /Ar	RE/Ar		Tb	Ce	RE lines and ring	Stage heater	Discharge	Reflected	
MAC	CeORSO-27	Quartz	1	20	5	2.0	0	210	220	100	504	4	60
ECR	CeORSO-28	Quartz	1	20	5	2.3	0	210	220	100	504	4	60

There are several important parameters to note in these growth tables. Firstly, samples CeORSO-27 and CeORSO-28 were grown several months prior to the start of this research project by a previous member of the research group. During the growths of the samples, terbium contamination in the lines and rings was a major issue in the CVD systems. Thus, despite the terbium cell temperatures remaining at room temperature (approximately 22°C) residual terbium in the deposition systems resulted in significant “contamination” in the films. [25] While this was originally viewed as an unfortunate accident, these films turned out to have valuable and comparable properties for use in this research project. Secondly, although the deposition times vary drastically (due to variations in deposition rates, between the two ECR PECVD systems), the thickness of all films was between 800-2000Å. The ratio of oxygen to silane gas flow rates was maintained consistently at roughly 10:1, while the argon flow was kept constant at 5sccm throughout. Finally, samples 007 and 008 were grown simultaneously on glass slides and n-type 100 silicon, respectively in order to have comparable samples for optical analysis.

## **ii. Overview of annealing techniques**

After deposition, samples were annealed in a quartz tube furnace. Previous experiments showed that annealing at 1200°C was sufficient to initiate the formation of cerium disilicate nano-structures in the film, and sensitize the Tb<sup>3+</sup> ions to emit at a wavelength of approximately 550nm (See section on Luminescence from Rare Earth Ions for the exact mechanisms involved). Past results also suggested that longer annealing times resulted in higher intensity photoluminescence. [25] Thus, isothermal annealing studies were performed to determine trends related to anneal times and rare earth concentration.

The samples were cleaved into squares using a hand-scribe (for silicon substrates) or a dicing saw (quartz and glass slide substrates) and annealed under a N<sub>2</sub> flow. Prior to the anneal, the quartz tube was rinsed and purged for an hour, and in order to reach 1200°C, the temperature was ramped up in 200°C increments (measured using a thermocouple) over 6 hours. A square from each set of samples (000, 001, 002, etc.) was annealed for 60, 120, 240, and 480 minutes respectively, with the exception of samples CeORSO 27 and CeORSO 28, of which only enough material was available for a single 480 minute anneal. Additionally, samples G007 and G008 that were grown on glass slides were not annealed due to the damage caused to the glass substrate at high annealing temperatures. A photograph of the annealing equipment set up is shown below.

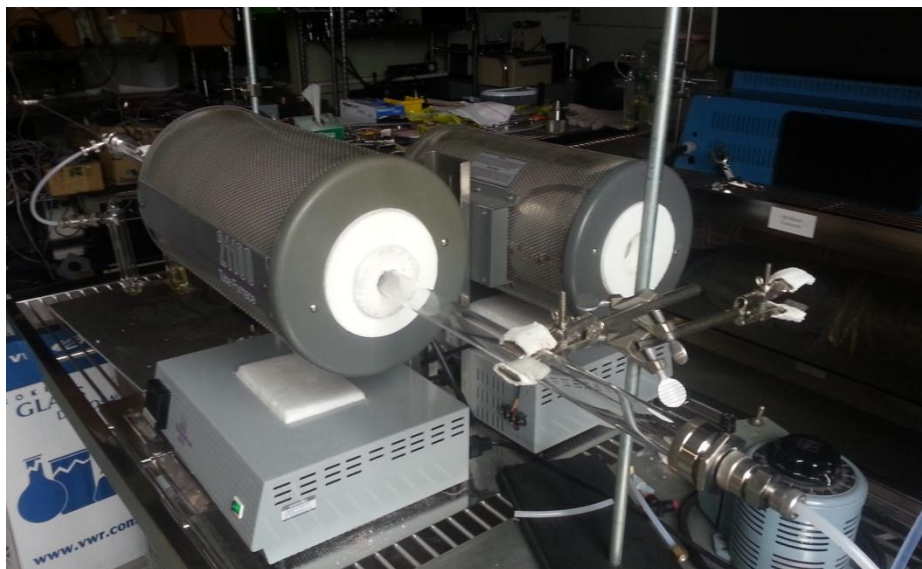


**Figure 17: Annealing furnaces with quartz tube holders. Furnaces were heated to 1200°C and ambient N<sub>2</sub> flowed over the samples during the annealing process.**

## b) Characterization Techniques

### i. Rutherford Backscattering Spectrometry

In order to determine the rare earth and other elemental concentrations in the films grown using ECR PECVD, the films were analysed using the Rutherford Backscattering Spectrometry (RBS) facilities at Western University in London, Ontario. A schematic diagram of this equipment is shown in Fig. 18 below:

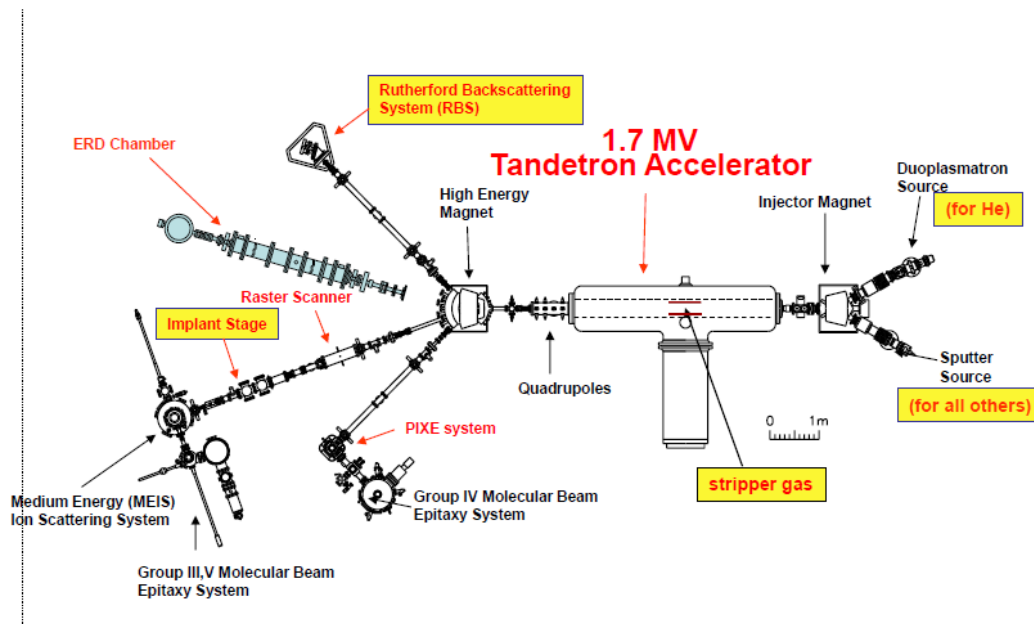


Figure 18: Tandem Ion Beam at Tandemron Lab, Western University [30]

The RBS technique involves bombarding a sample with high energy  $^4\text{He}$  ions and measuring the energy of the resulting elastically backscattered ions. There are many different types of ion-solid interactions, each lending themselves to a different type of characterization technique. Some of these interactions and the associated characterization techniques are summarized schematically below:

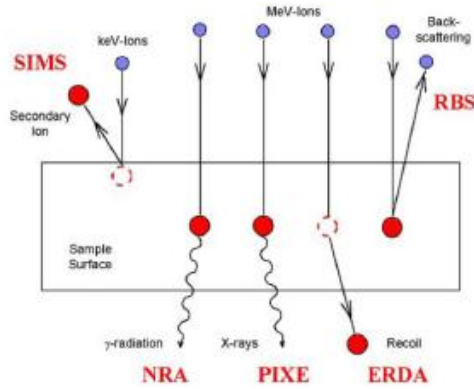


Figure 19: Ion-solid interactions [30]

The backscattered projectile energy measurement can be used to determine the composition and thickness of the sample with excellent sensitivity (on the order of parts per million) and depth resolution (on the order of  $\mu\text{m}$ ) [31]. The incident and projectile geometries are shown schematically below. The Tandetron Laboratory facilities are equipped with a 1.7MV tandem ion beam and use the Cornell geometry for RBS measurements, where the incident beam, exit beam and rotation axis are in the same plane. These parameters are related by the equation  $\cos(\beta) = -\cos(\alpha)\cos(\theta)$  and are shown schematically below.

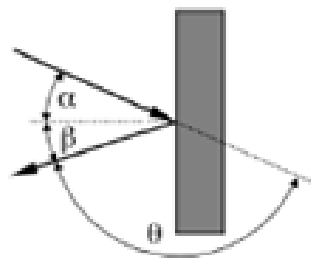


Figure 20: Incident and backscattered ions during RBS, in the Cornell geometry. [30]

The kinematic factor  $K$  determines the energy of the projectile, expressed by the equation

$$E_1 = KE_0$$

This kinematic factor term is dependent on the mass of the incident ion as well as the mass of the ions in the sample. It is given by the equation:

$$K = \frac{M_1^2}{(M_1 + M_2)^2} \left\{ \cos \theta \pm \left[ \left( \frac{M_2}{M_1} \right)^2 - \sin^2 \theta \right]^{1/2} \right\}^2$$

From this equation, it is apparent that the maximum scattering angle occurs when  $K=1$  and  $\theta = \sin^{-1} \left( \frac{M_2}{M_1} \right)$ . There is a much greater separation between energies for a small  $M_2$  (i.e. for a light target atom) because of a higher energy transfer between the particles. Therefore the RBS technique is better equipped to distinguish between heavy elements than light ones. [32]

The detector is sensitive to the energy of the backscattered ions, allowing it to determine the composition of the sample. As the ions travel through the target, they lose energy through collisions with the target atoms nuclei and electrons. The change in energy,  $dE$  after the ion passes a distance of  $dx$  in the material is known as the stopping power of the target. The “spread” of the peaks is due to the fact that backscattered projectiles are not mono-energetic but have a statistically determined range of energies. This is known as energy straggling and can limit the mass and depth resolution of the measurement. [32]

Additionally, the detector measures the number of backscattered projectiles which is dependent on the concentration of a specific element in the sample and the backscattering cross section of its nucleus. The backscattering cross section is directly proportional to the atomic weight of the elements, so heavier elements have a higher cross section than light ones and hence have a higher probability of a collision. This is shown by the equation below [30]:

$$\frac{d\sigma}{d\Omega} = \sigma(\theta) = \left( \frac{Z_1 Z_2 e^2}{4E \sin^2 \left( \frac{\theta}{2} \right)} \right)^2$$

In this equation  $E$  is the energy of the ion beam, and  $Z_1$  and  $Z_2$  are the atomic masses of the projectile and target respectively. Thus RBS is more sensitive to heavy elements (although as discussed above the detector may have more trouble distinguishing between two heavy elements than two light ones). [32] The thickness of a sample can also be determined from an RBS measurement, by measuring an elemental peak and dividing by the energy loss of the incident ion per unit depth in that particular element.

Unless otherwise specified, all measurements were made with a 1.5-2 MeV  $\text{He}^{4+}$  ion beam source. A silicon sample, implanted with antimony (Sb) sample was used as the standard to calibrate the detector. The detector resolution was 15keV and all data analysis was performed using the SIMNRA software developed by Dr. Matej Mayer at the Max-Planck Institute for Plasma Physics in Germany. [33]

## ii. Ellipsometry

Optical measurements were made using a J.A. Woollam Variable Angle Spectroscopic Ellipsometer. Ellipsometry is a non-destructive technique used to measure optical properties of thin films by measuring the change in the polarization of the incident light beam after passing through or reflecting from the material. Specifically, it measures two parameters:  $\Psi$  (amplitude ratio) and  $\Delta$  (phase change). The change in these two measured parameters can be used to determine a wide range of information, including thickness, surface roughness, uniformity, refractive index and crystallinity of the sample. The versatility of this technique, and its ability to measure a wide range of properties that depend on polarization changes makes it a popular choice in many industries, including medicine, optical coatings, and telecommunications research.

As an electromagnetic wave, the electric field vector of light propagating in the z-direction has both x and y components. Polarized light occurs when the x and y components have a consistent phase difference and therefore trace a consistent “shape” as the wave propagates through space, as is shown in Fig. 21.

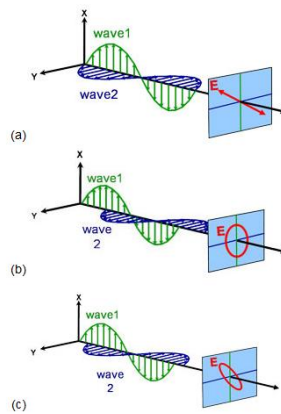


Figure 21: Linear, Circular and Elliptical polarization of the electric field vectors of propagating light waves. [32]

Materials with a refractive index higher than air cause incident light to slow down when passing through the sample, thus creating a frequency shift. This is described by the equation below:

$$v = \frac{c}{n}$$

The absorption coefficient describes the decrease of light intensity through the sample due to absorption. It is described by:

$$\alpha = \frac{4\pi k}{\lambda}$$

The loss of intensity is related to the absorption coefficient by Beer’s Law:

$$I = I_0 e^{-\alpha x}$$

It is dependent on the absorption coefficient as well as the thickness of the sample. Material properties are determined by measuring the intensity and polarization of light reflected from the sample. In an ellipsometry measurement, linearly polarized light is incident on a sample, inducing phase and amplitude changes in the incident beam due to the difference in refractive indices in the ambient medium (air) and the sample. The reflected light is now elliptically polarized as shown in Fig. 22.

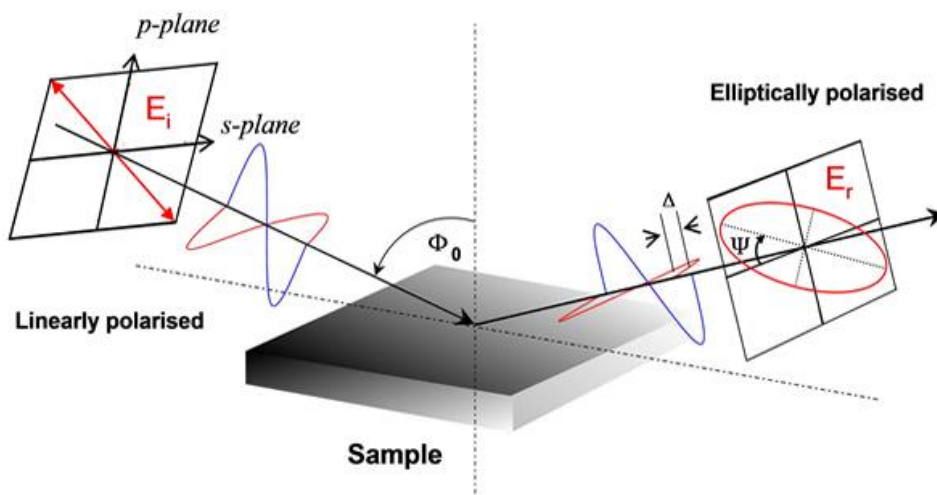


Figure 22 Incident and reflected beams during an ellipsometry measurement on a thin film sample [34]

Although ellipsometry uses thickness and refractive index measurements to characterize the sample, it does not measure these parameters directly. Rather, it measures the relative amplitude difference,  $\Psi$  and the phase shift,  $\Delta$ , as shown schematically in Fig 22. Deriving material parameters of interest involves modelling the optical response of the sample and its substrate and comparing it to experimental data, using a regression analysis technique. The model compares predicted values from the specified materials to the measured data using the Mean Square Error (MSE) to differentiate between the curves.

In the first set of ellipsometry measurements the refractive indexes of the as-deposited (AD) and 480 min annealed films were measured. The goal was to determine if there was a trend in refractive index as a function of rare earth concentration and annealing time. Past experiments suggested that the refractive index increased linearly with increasing rare earth concentration. These experiments also suggested that this trend was only evident in annealed samples, as cerium disilicate nanostructures do not form at low temperatures or short anneal times.

In order to perform these measurements, samples were mounted on the built in sample stage in the ellipsometer and aligned by ensuring the reflected beam passed into the centre of the detector. Measurements were made over the wavelength range  $250\text{nm} < \lambda < 1600\text{nm}$  at five different angles ( $55^\circ$ ,  $60^\circ$ ,  $65^\circ$ ,  $70^\circ$ ,  $75^\circ$ ) for a 2 second acquisition time. Measured data was modelled using Complete Ease spectroscopic software, based on the Cauchy model, as the film was transparent and Kramers Kronig consistent. Note that Kramer's Kronig consistency was maintained by applying the "Use KK mode" in the model. This constrains the optical constants to a physical regime (i.e. they are physically possible parameters), and reduces the total number of fit parameters, thus providing further confirmation that the optical constants are accurate. [35]

The model was then used to generate data that was assessed for the accuracy of its fit with the measurements. The model was determined to be a good fit with the data if the Mean Square Error (MSE) was lower than 20. A representative spectrum and model are shown below, to illustrate the salient features of the model.

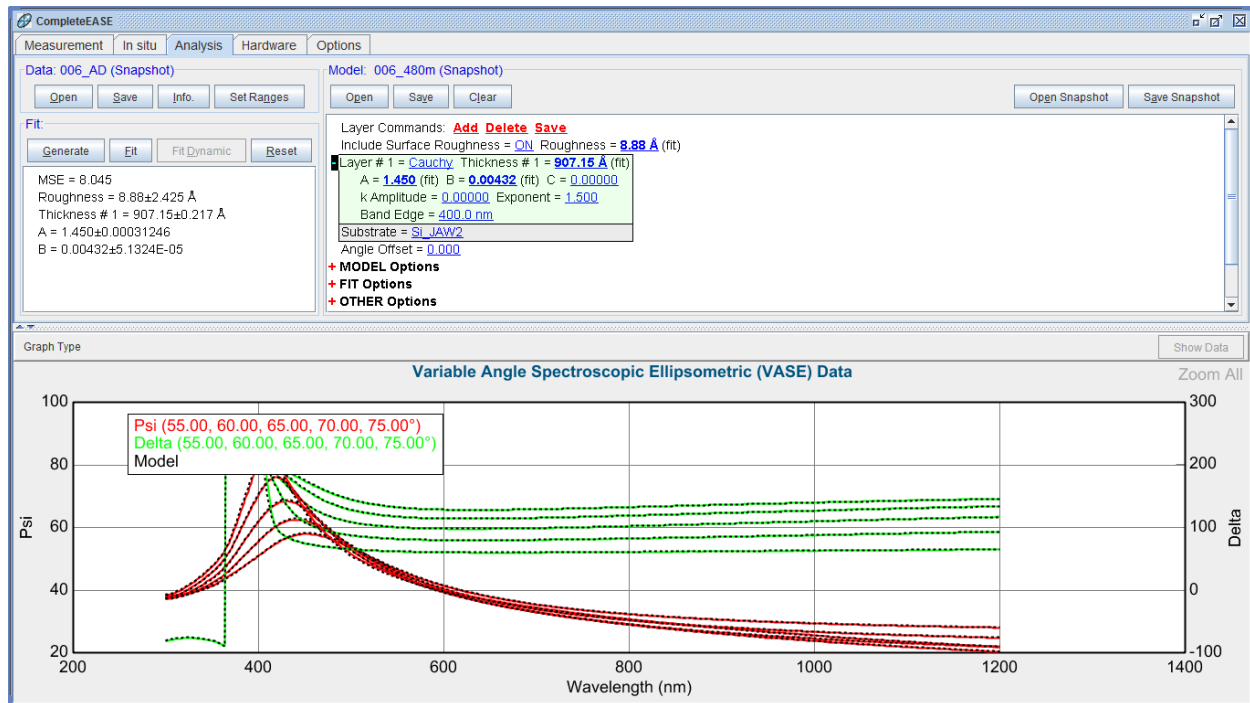


Figure 23: Complete EASE ellipsometry model of Sample 006 annealed for 480 minutes. Note the low Mean Square Error of 8.04 using a Cauchy model.

The fit parameters used in this model were surface roughness, layer thickness and the optical constants A and B that determine the refractive index as per the equation

$$n(\lambda) = A + \frac{B}{\lambda^2} + \frac{C}{\lambda^4}$$

The substrate model used was based on an existing library template, Si\_JAW2. The model shows good agreement with the measured data and the MSE is well below 20. Modifications were made to the film layer in films that exhibited anisotropy, or grading, and it was assumed that there were no backside reflection effects for the films grown on the silicon substrates.

### iii. Transmission ellipsometry

Transmission ellipsometry measures the intensity ratio, T given by the equation:

$$T = \frac{I_t}{I_i}$$

In this equation,  $I_t$  and  $I_i$  are the transmitted intensity and incident intensity respectively at each wavelength. The process for acquiring transmission measurements is very similar to that of other ellipsometry measurements to obtain optical constants. However, instead of mounting samples on the sample holder, they were mounted on the secondary “arm” of the ellipsometer so that the beam was incident perpendicularly upon the sample. This is shown schematically below.

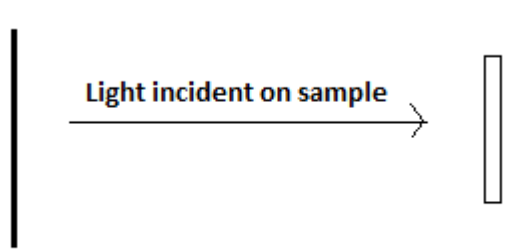


**Figure 24: Transmission ellipsometry experimental set up, showing 90° incident angle**

Samples grown on transparent substrates (glass slides and quartz wafers) were mounted on the detector arm using magnetic clips. The sample was aligned to ensure the spot was passing directly through the centre of the sample, and a standard transmission measurement recipe for a dielectric film on a transparent substrate was selected [35]. Once again, measurements were made over the wavelength range  $250\text{nm} < \lambda < 1600\text{nm}$ , but only at a perpendicular angle of incidence.

#### **iv. Photoluminescence**

Photoluminescence (PL) measurements were made at room temperature, using a 2mW, 325nm HeCd laser, and a USB2000+ spectrometer (previously calibrated using a tungsten halogen lamp) was used to measure emitted light. During PL measurements, the samples were excited to a higher energy state by absorbing high energy photons, which then decays to a lower

energy state by emission of a photon. The absorption and emission wavelengths are determined by the bandgap and absorption/emission bands of the sample being measured.

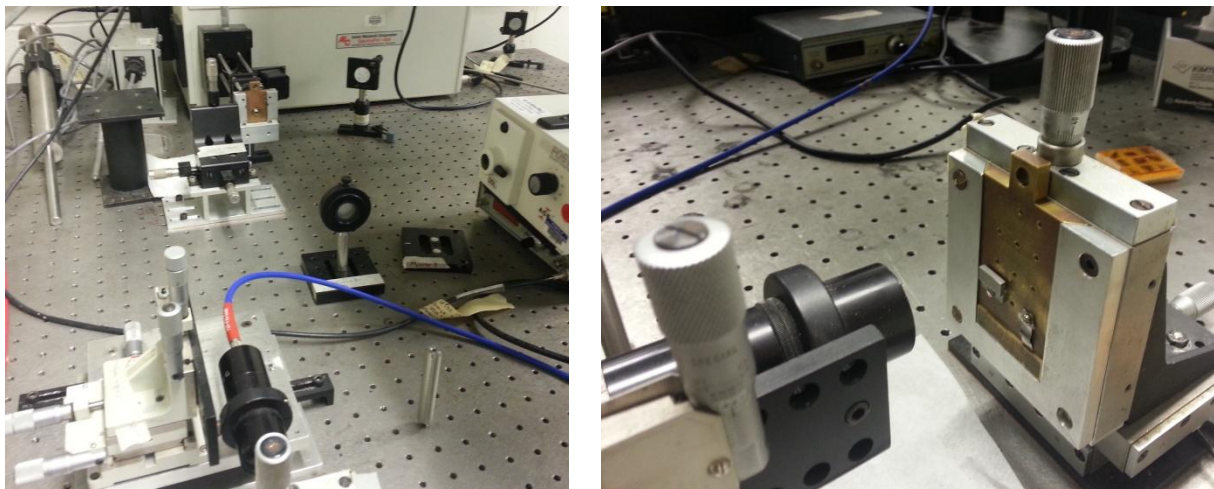


Figure 25: Photoluminescence equipment set up at McMaster University, CEDT Labs. Aligned mirrors are used to direct a 325nm He-Cd laser towards a sample holder, and light is collected through an Ocean Optics spectrometer

The goal of PL measurements was to determine the wavelength of peak emission intensity and to determine if there were any other secondary peaks. Past experiments suggest that the primary mechanism of emission should originate from energy transfer to the  $Tb^{3+}$  ions, and peak intensity should be at approximately 550nm. Secondary peaks may appear around 400nm, due to emission from cerium disilicate nanostructures. [25] The peak intensities of the LDS films were measured to identify any trends resulting from annealing conditions and rare earth concentration. Intensity was recorded as “arbitrary units” vs. wavelength.

#### v. UV-Vis Absorption Spectroscopy

For absorption spectroscopy measurements one illuminates the samples with light in the wavelength range of 200-1200nm, using tungsten filament and deuterium lamps. The reduction in the intensity of the light after passing through the sample can be used to determine material

properties, thickness and sample composition. Since composition and thickness were already determined using RBS and ellipsometry, only the absorption profile was measured using this technique. [36] A Cary 50 instrument equipped with a xenon arc lamp that can scan across 190-1100nm was used for these experiments.

Beer's law provides a quantitative relationship between absorption and the material properties of the sample as per the equation:

$$A_{\lambda} = \epsilon_{\lambda}bc$$

In this equation,  $\epsilon_{\lambda}$  is the molar absorptivity,  $c$  is the concentration and  $b$  is the path length of the beam to the sample (constant for all measurements). In order to obtain a reading from the detector, the system is calibrated by acquiring a 'dark current' measurement (a sample with 100% absorption) and then a blank measurement (0% absorption). The ratio of the sample's absorption with respect to these two measurements is used to determine its absorption profile. The detector in the system measures the excited state of the samples using a photomultiplier tube, upon absorbing an incident photon, producing a spectrum characteristic of the elements in the sample. [36] The system is illustrated schematically in Fig 26:

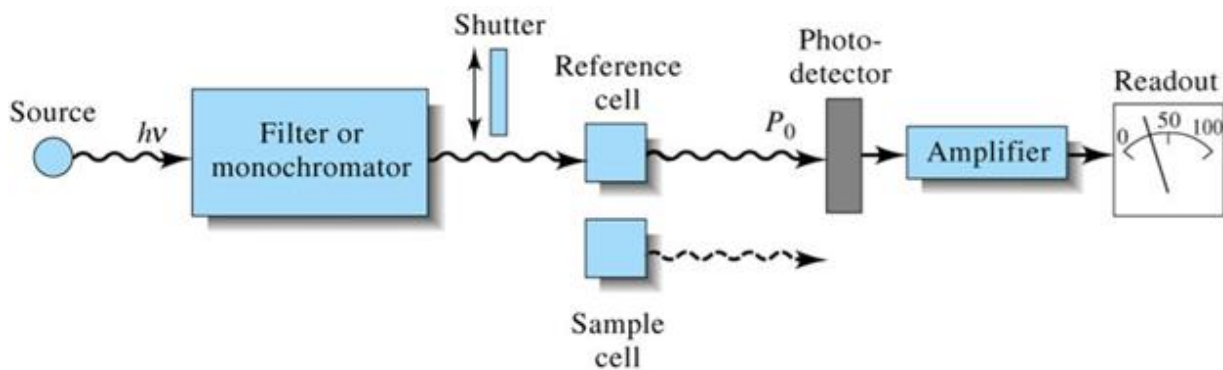


Figure 26: Set up of absorption spectroscopy equipment [36]

## vi. Pulsed Laser Deposition of CdTe

Pulsed laser deposition is a thin film deposition technique that uses high power laser pulses to vaporize and ionize a target in a process known as ablation. The ablated material condenses on a substrate where it creates a high quality thin film layer. The resultant film properties can be affected by several growth parameters such as laser fluence, spot size, repetition rate, chamber pressure and substrate temperature.

When the laser is incident upon the target (made of the same material intended to form the film, in this case pressed CdTe powder) it forms a plasma plume. The depth of penetration and thereby the plume formed are dependent on the material's attenuation coefficient and the pulse power of the laser. By controlling the chamber pressure, it is possible to control the plasma plume diffusion and direct it at a very specific target. Upon contact with the substrate, the plasma condenses and nucleates, controlled by changing substrate temperature. [37] The deposition chamber set up is shown schematically below.

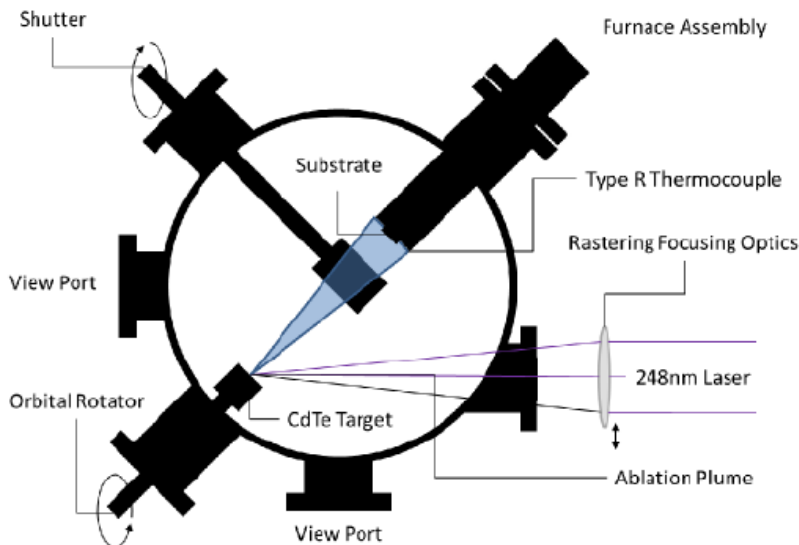


Figure 27: Pulsed Laser Deposition chamber during CdTe growth [37]

The substrates used were sapphire wafers, diced into 1cm x 1 cm pieces that were cleaned using acetone, isopropanol and methanol to remove any surface residues and debris. Once mounted in the chamber, but prior to deposition, the sapphire substrates were annealed for 30 minutes at 400°C. An excimer laser, that emitted at 248nm using KrF gas was used to create the plasma plume. During the deposition process, the voltage applied to the laser was varied from 28-39.9kV (in order to maintain an output power of 70-80mW), and growth occurred in 0.5Hz pulses for 120 minutes, at a chamber pressure of  $4.5 \times 10^{-7}$  Torr.

## VI. Results & Discussion

### a) Rutherford Backscattering: Sample Composition

Rutherford Backscattering Spectrometry (RBS) measurements were conducted at Western University in London, Ontario (as described in the “Materials and Methods” section) in order to determine the sample compositions. While growth parameters were chosen in order to achieve certain sample compositions and thicknesses, inconsistencies from previous growth sessions suggested a need to confirm sample composition post-deposition.

RBS measurements revealed five major elements in the samples: silicon, oxygen, cerium and terbium (in samples with heated rare earth cells during deposition) and trace amounts of argon from the carrier gas flow. A representative RBS spectrum showing these elements is shown below.

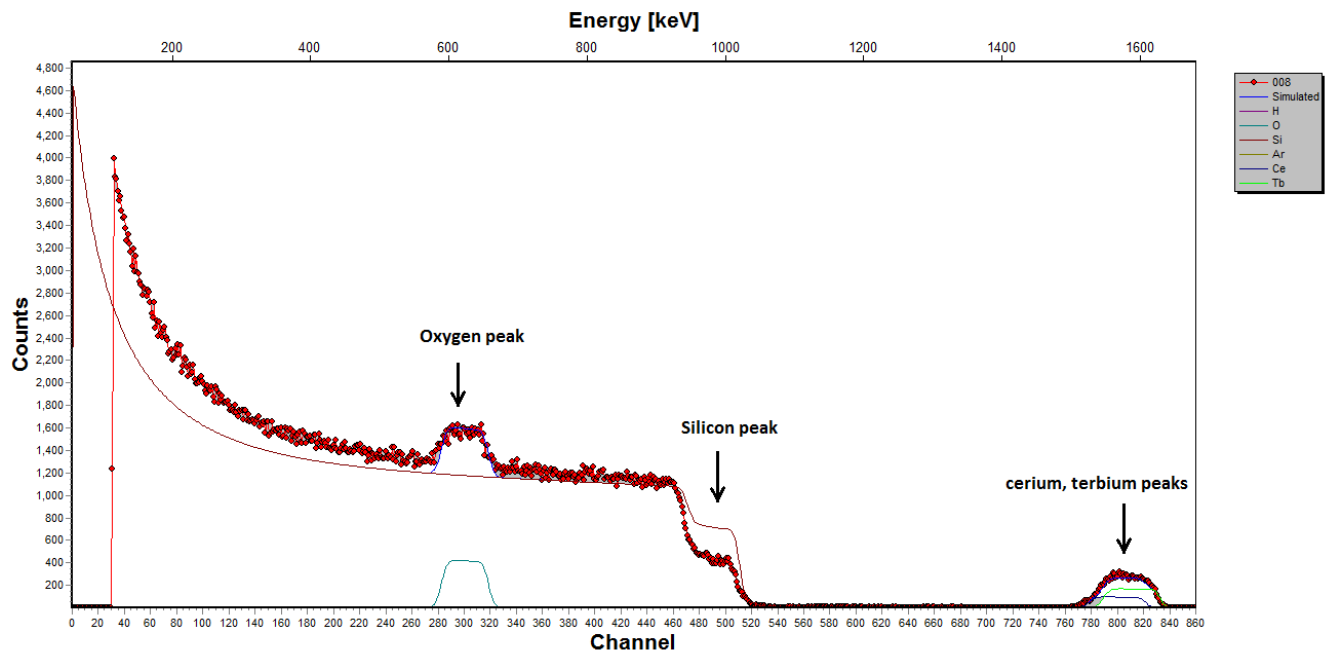


Figure 28: Representative RBS model of sample 005

The position of the peak on the x-axis is used to determine the elements present in the sample as they correspond to the energies of each element. The height of each peak corresponds to its concentration in the sample. Numerical concentration values are obtained by modelling the target as a series of layers of the substrate and the thin film. RBS analysis is a highly accurate measurement technique, routinely yielding uncertainties as low as 1% for heavy elements on light substrates. However, due to the low counts for the rare earth elements, the associated uncertainty was high. As RBS is a statistical method, the uncertainty is given by the equation:

$$\sigma = \sqrt{\frac{1}{N-1} \sum_{i=1}^N (x_i - \bar{x})^2}$$

That is, the uncertainty scales by approximately  $\frac{1}{\sqrt{N}}$ . Despite the higher accuracy of the *technique* for the heavy rare earth elements, their low concentration in some of the samples led to higher relative uncertainties. The uncertainty in the concentrations of Si and O has been estimated to be 1% based on past experiments [25] while the uncertainty of the rare earth elements is estimated to be (at least) 10%. Samples CeORSO-27 and CEORSO-28 were grown and analysed previously and their uncertainties are estimated at 1% for Si and O, and 0.1% for rare earth elements. Atomic concentration results are tabulated in Table 5:

**Table 5: Elemental composition of samples grown Note that the RE concentration of samples 000-004 is <0.1 at. %. Despite these essentially negligible concentrations, these samples were included in the data to illustrate general trends related to RE concentrations.**

Sample	Elemental composition (at. %)			
	Si	O	Ce	Tb
000	66.4	32.7	0	0
001	66.2	32.7	0.0007	0.001
002	66.0	33.0	0.0007	0.001
003	65.9	32.7	0.0006	0.002
004	66.6	33.3	0.001	0.0263
005	66.6	32.1	0.1	0.22
006	63.7	35.8	0.01	0.22
007, G007	63.8	35.3	0.4	0.2
008, G008	63.6	35.3	0.42	0.33
CeORSO-27	65.94	25.89	7.90	0.26
CeORSO-28	66.41	32.07	1.23	0.29

The data in Table 5 shows a fairly consistent concentration of silicon and oxygen in the samples, ranging between 63-66% and 32-35% respectively. However the rare earth concentrations were significantly lower than expected. The goal was to incorporate a maximum of 1% Tb and 5% Ce into the films, but samples 000-008 exhibit a maximum of 0.33% Tb and 0.42% Ce. In fact, at lower cell temperatures, the rare earth concentration was almost negligible - it could be detected by RBS measurements, but did not contribute to the luminescent or optical properties of the sample. The low rare-earth concentration was initially attributed to depletion of the rare earth cells by high temperature growth in previous deposition sessions. However, the terbium cell was determined to be almost full and the cerium cell was refilled after growing

sample 003, and yet concentration levels remained low. Thus the low concentration is believed to be due to clogging in the rare earth delivery lines. Future growths and calibration should focus on increasing the temperature of the rare earth rings and lines in order to ensure that the vapour does not condense before reaching the chamber, thus reducing the concentration of rare earth ions available to be incorporated into the sample.

Previous depositions on the same systems (with refilled rare earth cells and (presumably) minimal line clogging) revealed an exponential trend between cerium cell temperature and atomic % incorporated into the sample, as shown below.

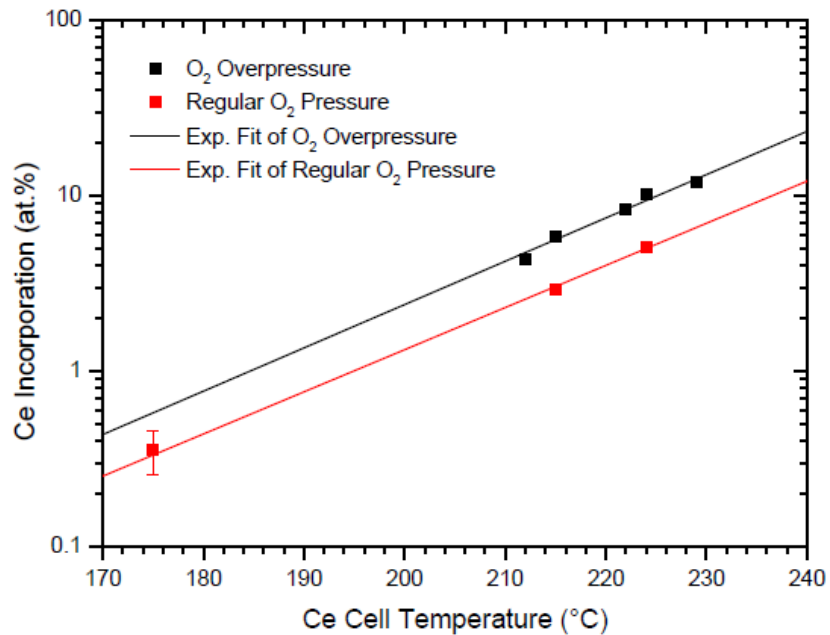


Figure 29: Cerium incorporation vs. cell temperature for previously grown samples. Similar data was not available for terbium incorporation. [25]

However, for the depositions 000-008, the relationship between cell temperature and rare earth incorporation was much less obvious, as is shown in Fig. 30 below. As mentioned previously, samples CeORSO-27 and CeORSO-28 were grown several months prior to samples

000-0008, by a different member of the research group, and thus system conditions may have differed significantly, under the same growth parameters. Cell temperature vs. rare earth incorporation for the set of samples used in this research project is shown in Fig. 30:

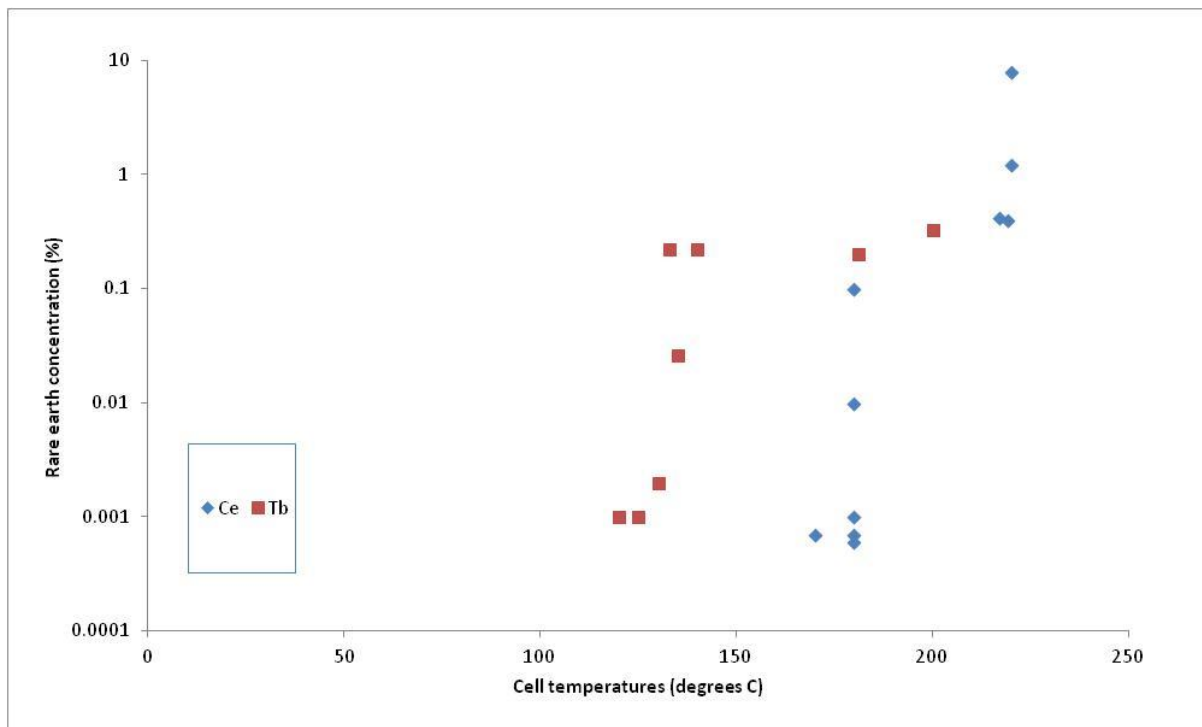


Figure 30: Rare earth incorporation vs. cell temperature for samples 000-008. There appears to be only a slightly discernible trend of higher incorporation with higher temperature.

Future growths should focus on optimizing rare earth concentration in the samples. Ideally, rare earth concentrations would have increased in consistent increments to a maximum of 1% Tb and 5% Ce, as these concentrations produced favourable results (i.e. high luminescence and sharp peaks) in previous sample growths [25] Currently, samples CeORSO-27 and CeORSO-28 serve as a demonstration of the optical and luminescent properties that could have been expected, given higher incorporation of Ce and Tb into the samples.

## b) Photoluminescence

Photoluminescence measurements were crucial to the characterization of the LDS films. In fact, the intensity and wavelength of emission would determine the success of the project as a whole: in order to be suitable for LDS applications on CdTe photovoltaic cells, the LDS layers would need to emit in the wavelength range of 500-750nm (See Fig. 10). Additionally in order to justify the application of an LDS layer, the emission intensity in the desired wavelength range must be sufficiently high to account for any losses resulting from parasitic absorption, emission away from the photovoltaic cell or recombination losses. While external quantum efficiency (EQE) measurements were not completed in time for this project, they would certainly serve as a valuable tool to quantify emission intensity and gauge if it was sufficient to justify application of the LDS layer.

As discussed previously, after deposition samples were cleaved and annealed at 1200°C for 60, 120, 240 and 480 minutes as well as left as-deposited, in order to study the effects of time during isothermal anneals. In fact, past experiments suggested that longer annealing times resulted in an increase in photoluminescence intensity due to the formation of more cerium disilicate structures. Since very little of samples CeORSO 27 and 28 was available, there was not enough of either to perform a complete annealing study. A cleaved sample CeORSO-27 was annealed for 480 minutes, while cleaved samples of CeORSO-28 were left as-deposited and annealed for 480 minutes.

The major sources of error in photoluminescence measurements arise from improper calibration of the Ocean Optics USB2000+ spectrometer and inadequate light capture from the sample. The spectrometer was previously calibrated using a tungsten halogen lamp, and this reference spectrum was used for all subsequent measurements. Mirror and sample positioning

was also calibrated when setting up the system so as to maximize light absorption by the spectrometer (i.e. ensure there were no extraneous reflections that would deflect the beam away from the spectrometer). These positions were not altered during photoluminescence measurements, however, there will always be an inherent loss mechanism involved in this process since the detector has a finite incidence angle and many photons are not emitted in the direction of the lens. Finally, a small but notable source of error is caused by laser instabilities: since these photoluminescence measurements were performed within days of each other, this effect was considered negligible between samples.

A literature search did not reveal any specific values related to uncertainties in photoluminescence measurements, however a great deal was found for quantum efficiency uncertainty measurements with similar set ups, but with an integrating sphere. As a conservative estimate, the uncertainty of the photoluminescence measurements was estimated to be approximately that of an external quantum efficiency measurement, at 1%. [38]

The graphs below show PL intensity (arbitrary units) as a function of wavelength for each set of samples. Due to the low rare earth concentrations in samples 000-003, PL emissions could not be distinguished from noise (essentially zero PL). A representative graph of sample 003 is shown in Fig 31 below, while the others have not been included for the sake of brevity.

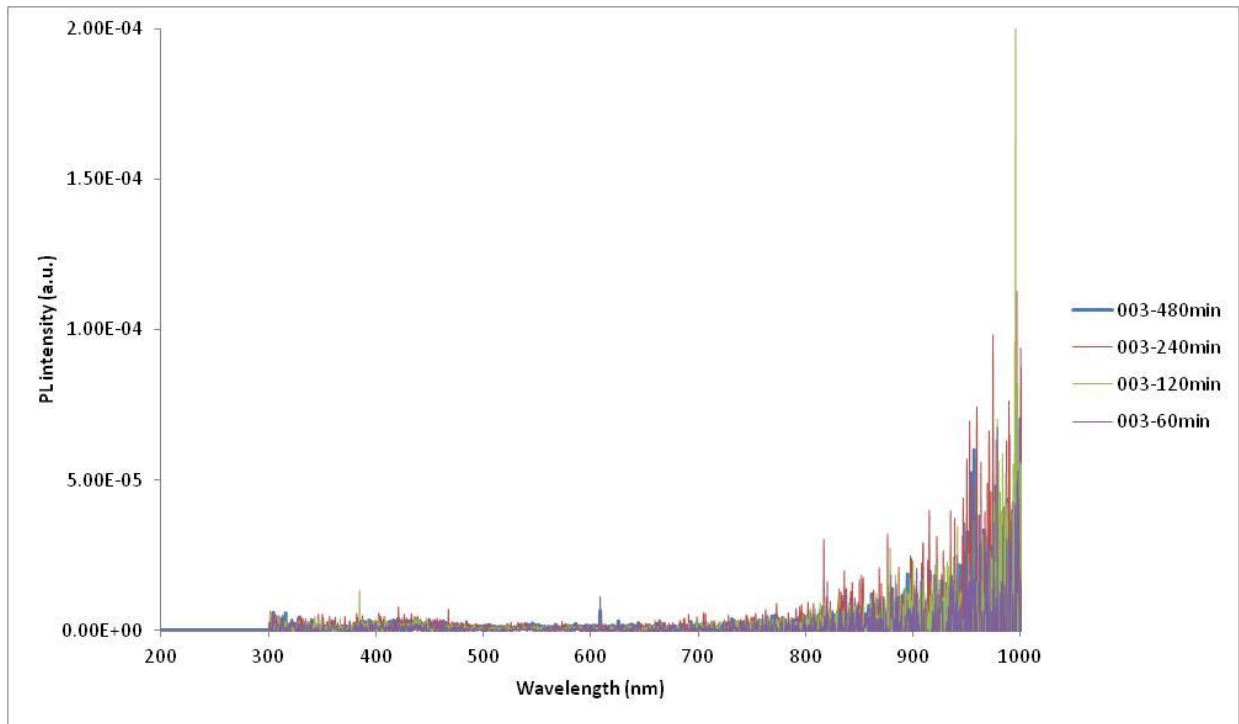


Figure 31: PL results for Sample 003, annealed from 60-480 minutes, showing minimal emission at any wavelength, likely due to very low rare earth concentrations.

As the rare earth concentration in the samples increased, specific peaks became more noticeable. Although sample 004 showed a peak around 650nm it was only at sample 005, that distinct rare earth peaks began to appear. This is shown in Figs. 32 and 33 below.

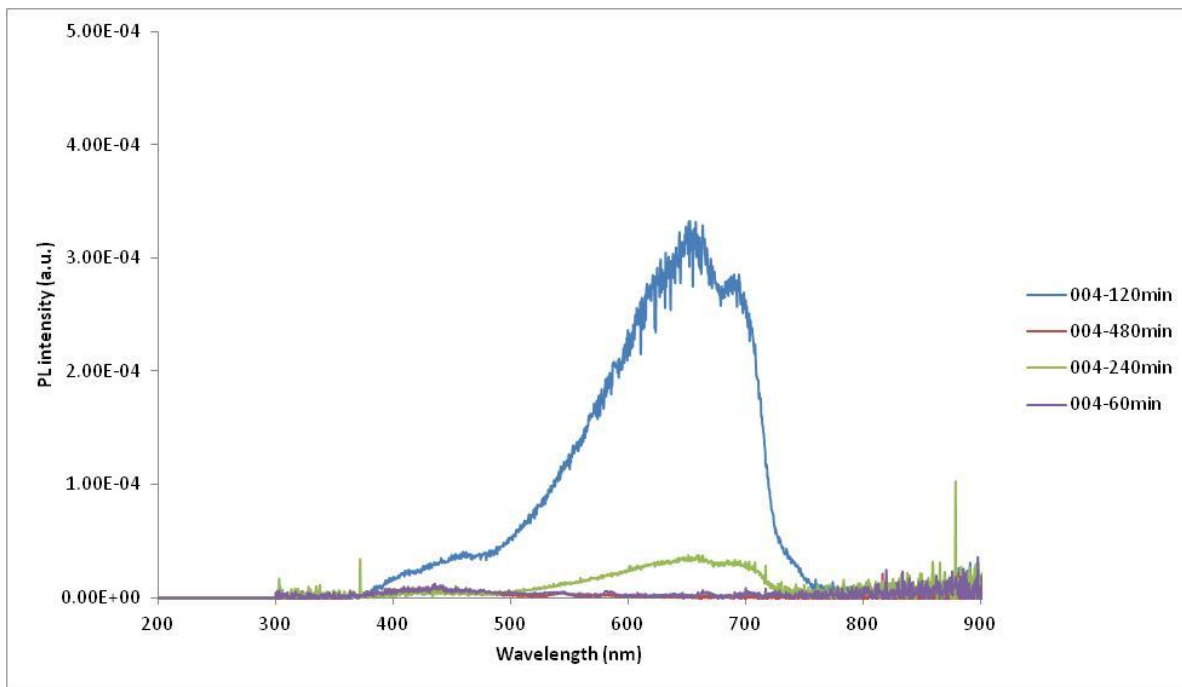


Figure 32: PL results from sample 004, showing a broad, and likely non-rare earth related peak at certain anneal times, but minimal overall luminescence.

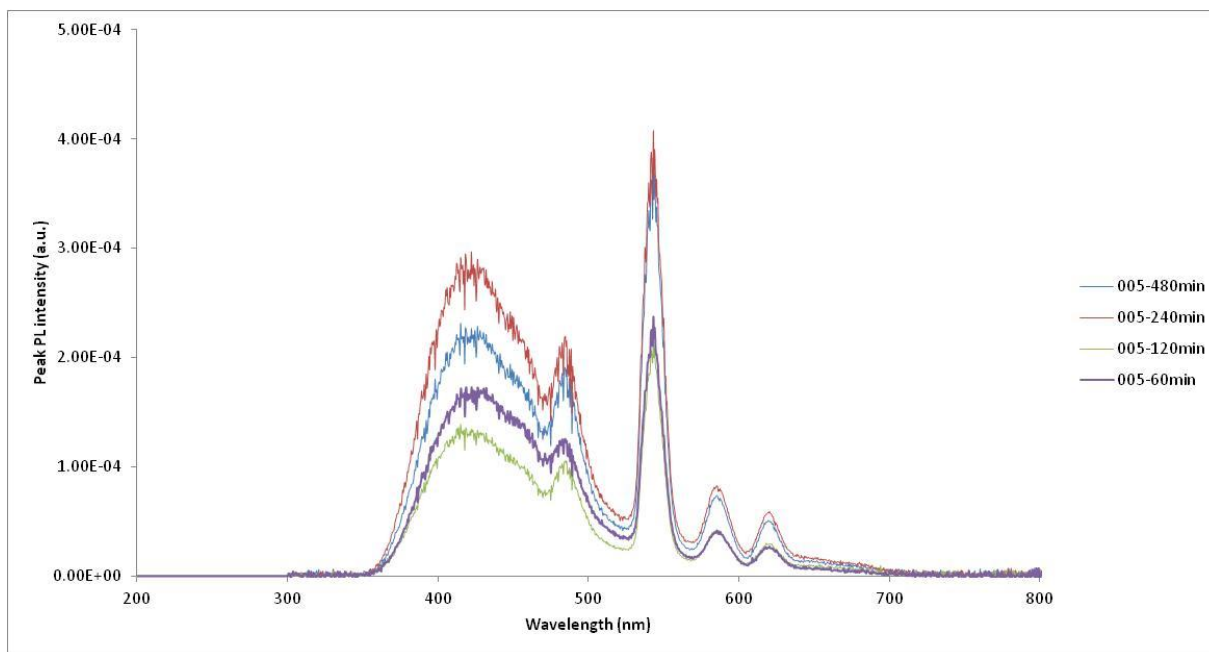


Figure 33: PL results from sample 005, showing distinct rare-earth related peaks around 400nm (Ce) and 550nm (Tb) for all annealing times

As discussed previously, the peak PL intensity in sample 005 occurs at approximately 550nm and is associated with  $Tb^{3+}$  emissions. The broader, lower intensity peak around 425nm is associated with cerium emissions. The 550nm peak is within the high EQE range for CdTe photovoltaics as discussed in the Introduction, however in order to justify the application of an LDS layer, there would need to be a more efficient energy transfer between the cerium disilicate nanostructures and the  $Tb^{3+}$  ions. Ideally, the cerium peak would be minimal with all of the energy transferred to Tb emissions, resulting in a higher intensity peak at 550nm. The higher PL intensity at high temperatures and longer anneal times is associated with a greater percentage of cerium converted to cerium disilicate, and thus greater absorption of incident light. XRD results on similar films revealed that at 1200°C, 95% of the nanocrystals in the film had converted to cerium disilicate structures. Furthermore, the grain size increased with higher annealing temperatures, without any noticeable change in phase. [25] For a full analysis of isochronal annealing trends and their impact on physical structure and nanostructure formation please refer to [25].

As the rare earth concentration increased, the peaks became more sharply defined and their intensity increased. Moreover, the intensity was directly related to annealing time- with only a few exceptions, PL intensity increased with annealing time, with most samples exhibiting highest PL efficiency after 240 minute or 480 minute anneals, as initially predicted. In all cases, the as-deposited samples exhibited no luminescence at all.

All samples annealed for 480 minutes are plotted on the graph in Fig. 34 below:

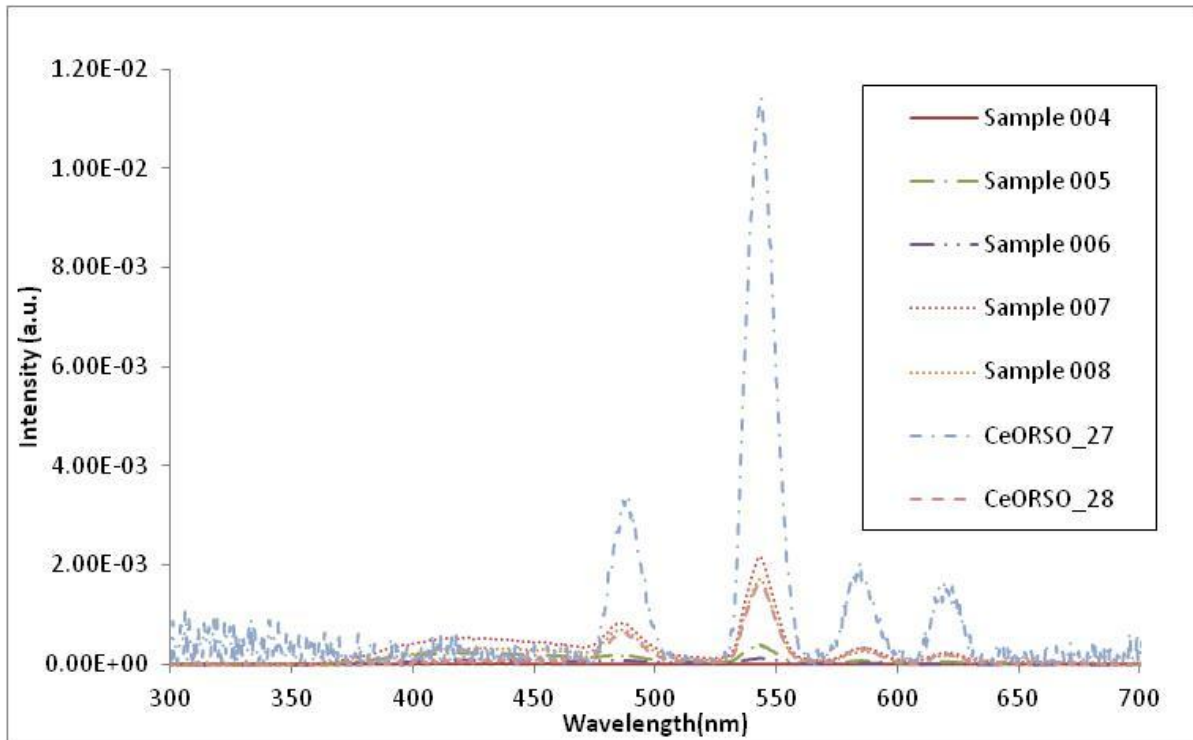


Figure 34: PL intensities for all 480minute annealed samples, showing a consistent trend of increasing intensity with rare earth incorporation.

This data reinforces that PL intensity is strongly correlated with rare earth concentration: sample CeORSO-27 (with Tb and Ce concentrations of 0.26% and 7.9% respectively) exhibits the highest PL intensity, with strong peaks also exhibited by samples 007 (0.2% Tb and 0.4% Ce) and CeORSO-28 (0.29% Tb and 1.23% Ce). As Tb concentrations increase, it is apparent that the cerium peaks (and other, extraneous peaks) reduce in intensity and become narrower, thus suggesting that energy is more efficiently transferred to the  $Tb^{3+}$  transition.

This set of photoluminescence experiments confirms the formation of cerium disilicate crystals at sufficiently high annealing temperatures and annealing times, and the subsequent energy transfer to the terbium ions, which emit at 550nm. While the trends are promising and confirm initial predications regarding PL intensity and sample composition, the intensity is still too low to be directly applicable for LDS applications. Thus, future sample growths should focus

on optimizing rare earth concentrations in the samples, with the possibility of incorporating as much as 5% Tb and 10% Cerium. Annealing experiments should focus on long (480 minute) anneals and ensuring that the furnace temperature is stable throughout the process.

### c) Ellipsometry

As described in the Materials & Methods section, ellipsometry measurements were made with the J.A. Woollam Variable Angle Spectroscopic Ellipsometer (VASE) system. Measured data was modelled using Complete Ease spectroscopic software, and used to determine refractive index vs. wavelength and the thickness of the films, as well as any grading or inhomogeneities in the layers. Accuracy in ellipsometry measurements is the error between experimental data (averaged to reduce noise) and theoretical values. Typically, in order to quantify ellipsometry accuracy, measured data is compared against known values of reference samples such as silica, silicon with native oxide and gold films. [39]

A Mueller matrix is a 4 x 4 matrix used to describe the transmission and reflection of light, using the Stokes vectors of the incident and reflected beams. The accuracy over a range of wavelengths, is quantified by the root mean square (RMS) between the measurements and the ideal elements of the Mueller matrix, defined in terms of the two measured parameters  $\Psi$  and  $\Delta$ . The three factors in the Mueller matrix are:

$$N = \cos 2\Psi$$

$$C = \sin(2\Psi) \cos \Delta$$

$$S = \sin(2\Psi) \sin \Delta$$

These three parameters can be used to determine the signal intensity  $I(t)$  after passing through the sample. Thus, the RMS error is defined by the measured values of  $N$ ,  $C$  and  $S$  and the ideal values,  $N'$ ,  $C'$  and  $S'$  as per the equation:

$$E = \sqrt{\frac{1}{3n} \sum_{i=1}^n [(N_i - N_i')^2 + (C_i - C_i')^2 + (S_i - S_i')^2]}$$

Using this method, the inherent error in a typical ellipsometry measurement is estimated to be approximately 0.1%. [39] However, in this case, experimental error played a much more significant role in the overall uncertainty of the measurement. Experimental error was due to contamination on the sample surface (as they were not cleaned prior to measurements) and alignment inconsistencies (as samples were manually aligned using stage knobs). These errors are estimated to be approximately 3% for a total compounded uncertainty of 3.1%

The refractive index at 632nm for the as-deposited samples vs. the total rare earth atomic concentration in each sample is plotted in Fig. 35 below. Earlier experiments suggested that there should be no correlation between rare earth concentration and refractive index for as-deposited samples. However, the data above shows a loose trend of increasing refractive index with RE concentration. This trend is slightly stronger with the annealed samples, also plotted in Fig. 35.

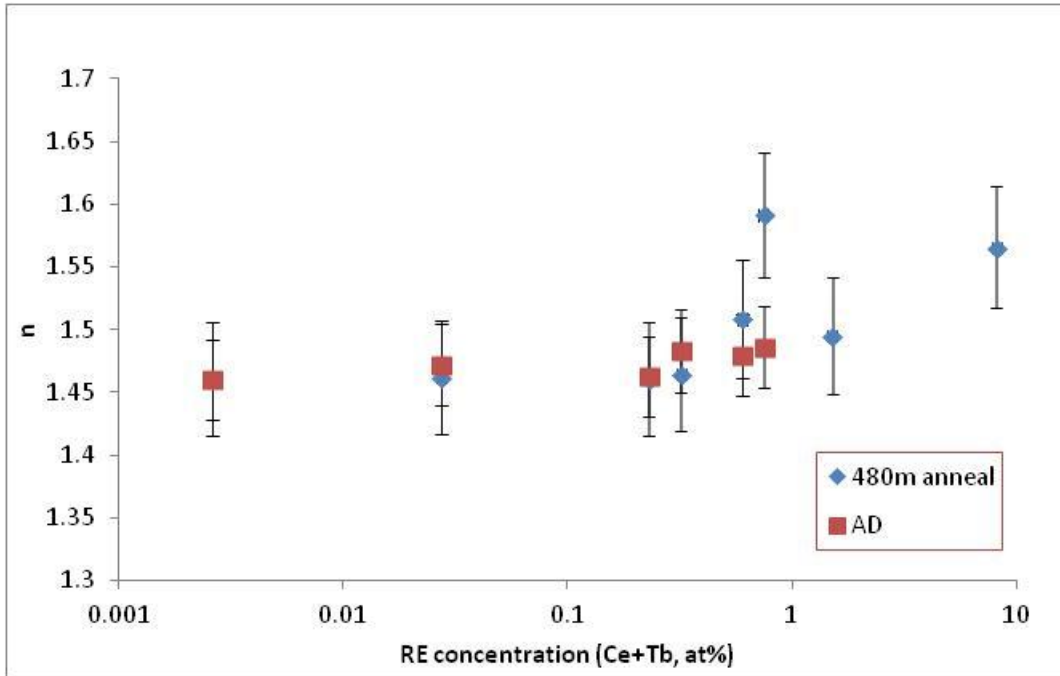


Figure 35: Refractive indices show a slight trend of increase with rare earth concentration for 480 minute annealed samples,

, There is a slight increase in the refractive index upon annealing, suggesting the formation of cerium disilicate crystalline nano-structures in the sample at high temperatures. Ellipsometry modelling also revealed several features of the LDS films themselves. The average thickness of the films was around 1200Å, and for the most part did not exhibit any grading. Modelling revealed that after annealing, samples 007 and 008 appeared to have two distinct layers comprising the LDS film.

#### d) UV-Vis Absorption Spectroscopy

Only specific films were chosen for absorption and transmission measurements. These films were chosen on the basis of high PL intensity and their substrate. In order to make absorption and transmission measurements, the LDS films needed to be grown on transparent

substrates to avoid interference and reflection effects. Also, transparent substrates were required to measure the absorption within the LDS films and CdTe layers.

On this basis, samples G007, CeORSO 27 and CeORSO 28 were selected. Since sample G007 was grown on a glass slide, it could not be annealed and therefore its absorption and emission properties will be different from the annealed films studied for PL and ellipsometry purposes. Future experiments should focus on re-growing samples on quartz so that they can be annealed before making absorption and transmission measurements. Samples CeORSO27 and CeORSO28 were chosen because of their high PL intensity and optimal rare earth concentrations, as past experiments showed that both exhibited strong luminescence. These samples were grown on quartz substrates.

Errors in UV-Visible absorption spectroscopy measurements are derived from a range of sources. Intrinsic uncertainty is due to the spectroscopy technique itself, but with proper calibration procedures, can be reduced to less than 1%. Instrumental uncertainties are due to instrument noise, temperature fluctuation, sample positioning and dust or other contaminants in the measurement chamber. Repeating measurements can help to eliminate some of these sources of error. Baseline and response drifts are another common source of error in most standard absorption spectrometers (apparent in the negative absorption measurements in Fig. 37) typically related to a change in the absorbance scale of the instrument. Finally, non-linear detector responses, while correctable, can also have a significant impact on the uncertainty. [40]

Chemical uncertainty sources arise from the samples being measured and are much harder to quantify. Typically, these uncertainties result from extraneous absorption, due to strongly absorbing contaminants in the sample that skew results. Since the samples were cleaned with methanol and acetone prior to the measurements and RBS analysis did not reveal the

presence of a significant concentration of contaminants, it seems safe to assume that this did not contribute significantly to the uncertainty. Other errors can arise from gradual chemical changes to the sample itself due to the wavelengths used for measurements. Once again, this specific material system is not known to be degraded by exposure to light in the UV-Visible wavelength, and thus this specific error was not an issue.

The combination of these components can be used to estimate a standard uncertainty of 7.5% for a typical absorption spectroscopy measurement, with chemical uncertainty making up the majority of the components. This estimate is likely excessive for the rare earth based samples used in this research project, since they were largely unaffected by chemical issues. Thus, a more conservative estimate of 5% is applied to these measurements.

#### **i. Absorption measurements**

The results of the absorption measurements for the three chosen samples are shown in Fig. 36. Note that the negative absorption shown for sample G007 is due to an uncorrected baseline on the absorption spectrometer and not indicative of a physical characteristic of the film. While a complete recalibration of the system could have been performed to correct the baseline, this was not undertaken during this research project. Future experiments should take this into consideration and the instrument should be recalibrated if possible.

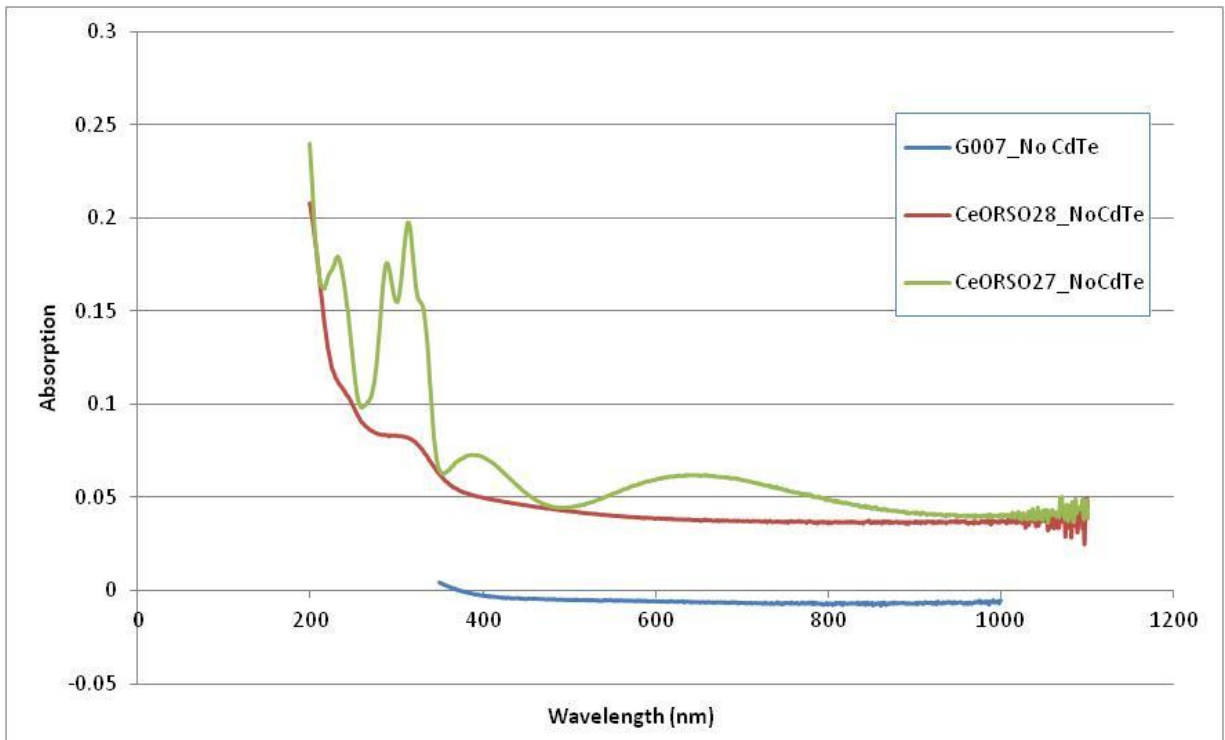


Figure 36: Absorption measurements for films G007, CeORSO-27, and CeORSO-28 show similar trends in absorption profiles but much stronger absorption in samples with higher rare earth incorporation.

The data shows that sample G007 exhibits very low absorption. As mentioned earlier, this is likely due to the fact that it is not annealed and therefore, did not form nanostructures, which are the primary absorption complexes in the LDS films. However, samples CeORSO 27 and 28 exhibit very strong absorption in the 200-300nm wavelength range, with a steep cut off in absorption at  $\lambda > 400\text{nm}$ , likely due to the relatively high concentration of cerium disilicate nanostructures that formed as a result of the significantly higher rare earth concentration in these films. Sample CeORSO27 in particular, with 7.9% Ce (as compared to 0.40% and 1.23% for samples G007 and CeORSO 28 respectively) exhibits sharp peaks in absorption at short wavelengths due to the formation of more nanostructures.

The high absorption regions of the LDS layers correspond to low EQE regions of the CdTe solar cell as shown in Fig. 10 Ideally, all photons at these wavelengths would be absorbed

by the LDS layer and then re-emitted at longer wavelengths where the cell performs more efficiently. The sharp cut off in absorption around 400nm corresponds to the region in which the EQE of a CdTe solar cell starts to increase, before peaking between 500-700nm. Thus, the reduced absorption by the LDS layer in this range suggests that when applied to a CdTe cell, there will be minimal parasitic absorption by the layer at wavelengths that can be efficiently absorbed and utilized by the cell itself.

Samples G007 and CeORSO28 were coupled with the thin film CdTe as shown in Fig. 37 below.

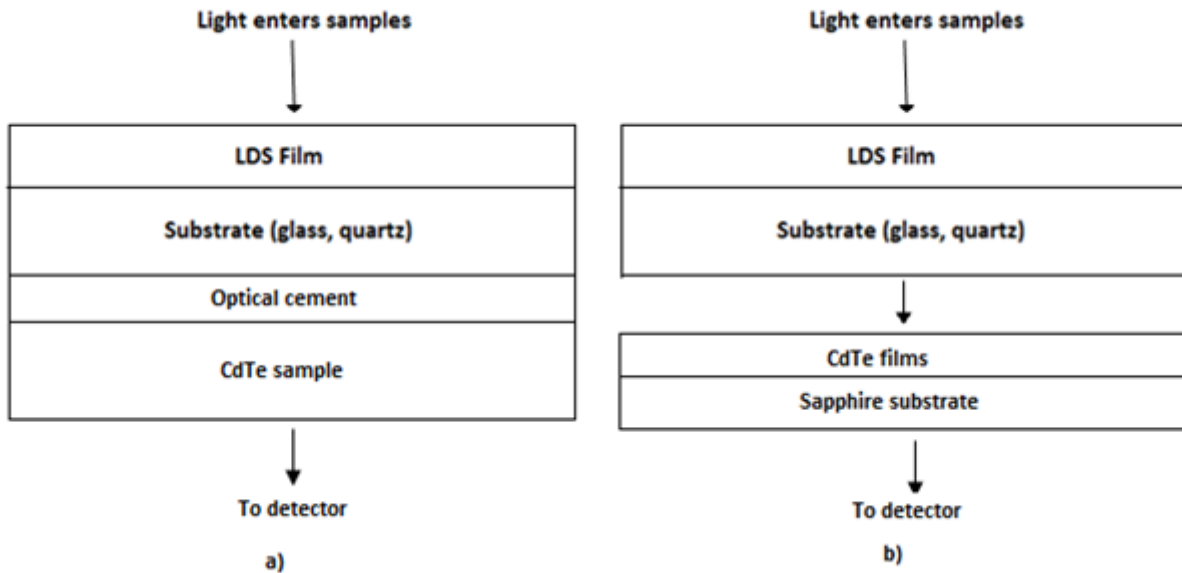


Figure 37: LDS sample coupling with CdTe films. In the case of samples G007 and CeORSO 28 the samples were mounted on CdTe using optical cement. Sample CeORSO-27 was manually stacked on top of the CdTe film as there was very little of the sample left for future experiments.

Absorption measurements were made by measuring the light passing through the sample in order to determine the absorption properties of the CdTe in combination with the LDS films. With an ideal LDS layer, there would be strong absorption in the short wavelength range (200-300nm) due to absorption by the nano-structures. CdTe effectively absorbs photons in the 500-

700nm range, so the absorption in this region should be unaffected. Thus, absorption curves are expected to exhibit a sharp peak at shorter wavelengths and a decrease in absorption at  $\lambda > 400\text{nm}$ . However, interface reflection effects and parasitic absorption by the substrate may contribute to deviations from this ideal absorption spectrum.

The results of absorption measurements for sample G007 on a glass substrate mounted on CdTe is shown in Fig. 38, compared with sample G007 without the CdTe films.

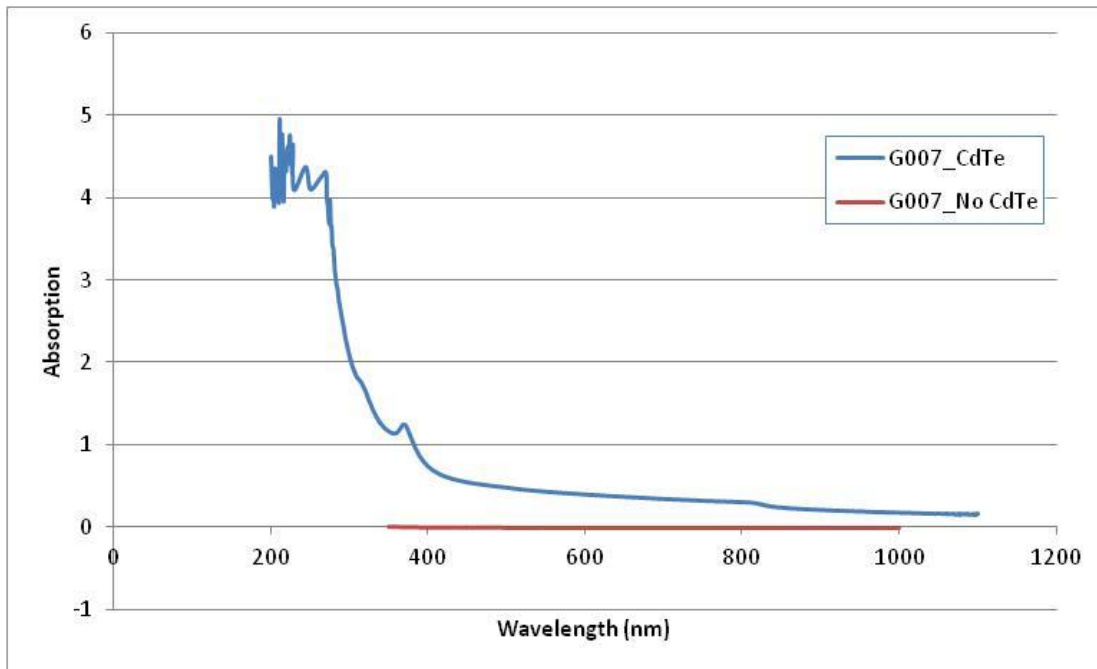


Figure 38: Results of absorption measurements of CdTe coupled with sample G007, compared to that of sample G007 with no CdTe

Since there is little to no absorption by sample G007 as indicated by Fig. 36, the high absorption at  $\lambda < 400\text{nm}$  can be largely attributed to the intrinsic absorption of the CdTe sample. Similar measurements were made for sample CeORSO 28 mounted on CdTe. As indicated in Fig. 36, CeORSO 28 demonstrated much stronger absorption than sample G007. Absorption measurements for CeORSO-28 are shown in Fig. 39.

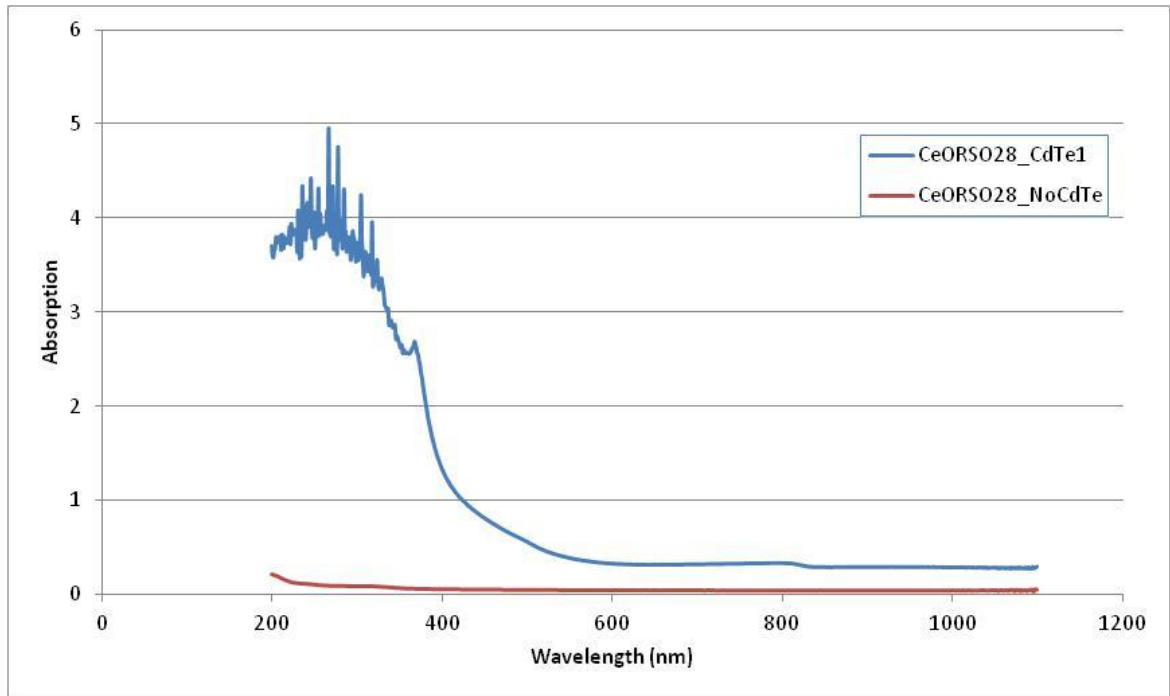
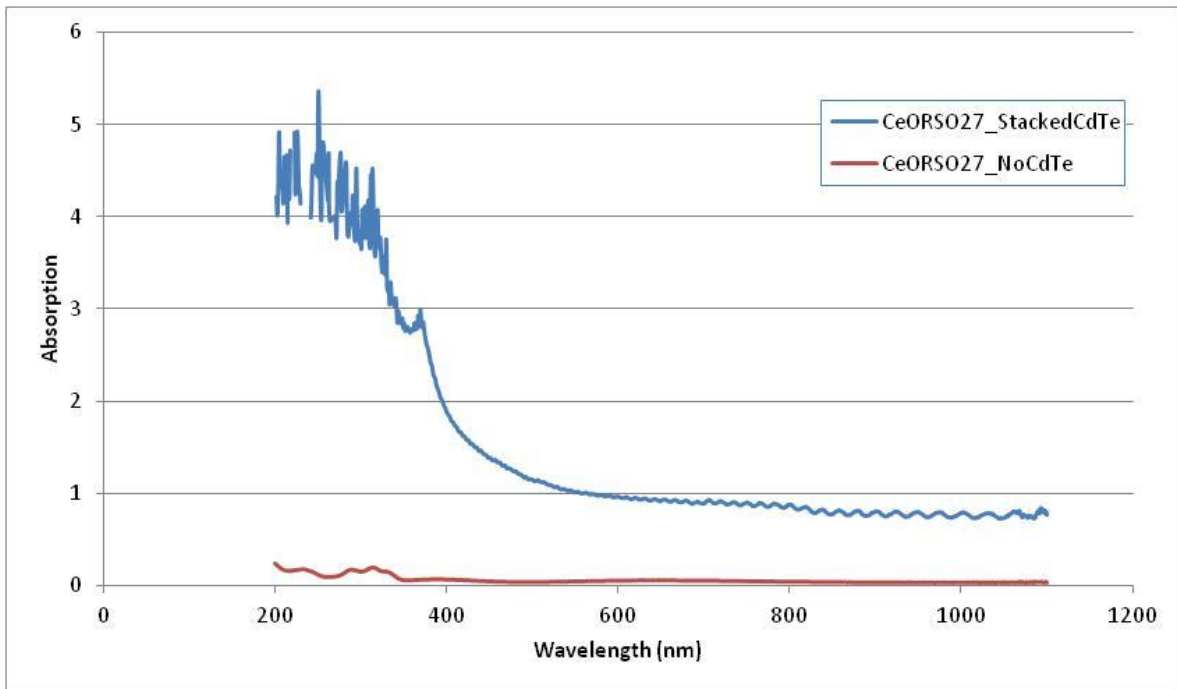


Figure 39: Results of absorption measurements of CdTe coupled with sample CeORSO-28, compared to that of sample CeORSO-28 with no CdTe

Some of the strong absorption at short wavelengths through the system can be attributed to the LDS layer as well as the CdTe film. Measurements for CeORSO27 on CdTe yielded similar results, as shown in Fig. 40.



**Figure 40: Results of absorption measurements of CdTe coupled with sample CeORSO-27 mounted on CdTe, compared to that of sample CeORSO-27 with no CdTe**

Once again, the relatively strong absorption exhibited by this sample likely contributed to the overall strong absorption through the system. While the results for all three absorption measurements reveal very similar trends (and a significant portion of the absorption spectra can likely be attributed to the CdTe layer) since sample CeORSO27 was ‘stacked’ as shown in Fig. 37b, (i.e., not mounted using optical cement), interface reflection effects could have also contributed to the absorption spectra. If repeated, this sample should be mounted like samples G007 and CeORSO28 to mitigate these effects.

## ii. Transmission ellipsometry

Transmission measurements were made using the previously described Woollam Ellipsometer. The transmission measurements for samples G007, CeORSO 27 and CeORSO 28 are shown in Fig. 41.

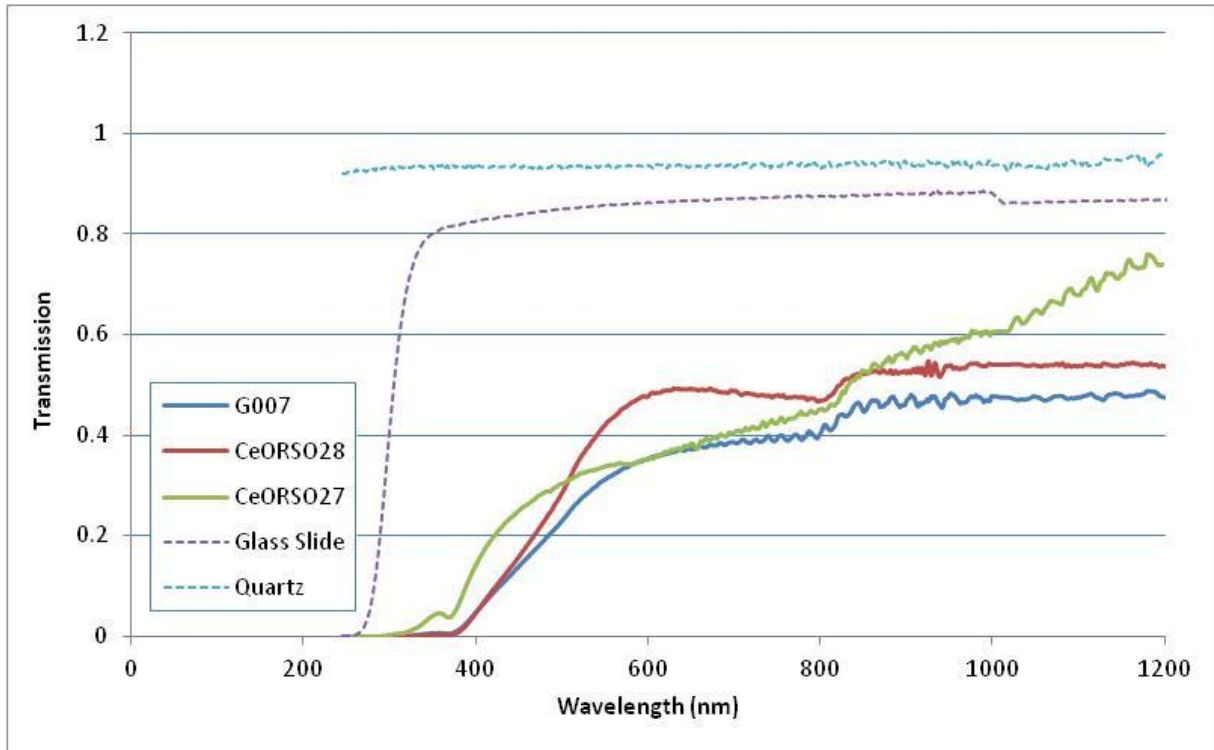


Figure 41: Transmission ellipsometry measurements- comparison between Samples G007, CeORSO-27 and Ce-ORSO-28 and their quartz and glass slide substrates

In addition to the transmission spectra for the LDS films the graph above also shows the transmission curves of the glass slide substrate (G007) and the quartz substrate (CeORSO27, 28). When compared to its substrate, the transmission spectra of sample G007 is very similar, exhibiting a sharp cut off in transmission around 300nm. This confirms the previous theory that absorption by sample G007 is minimal as it is un-annealed. Any absorption exhibited by the sample is likely due to absorption by its substrate. In comparison, samples CeORSO27 and 28

exhibit significantly lower transmission (suggesting strong absorption) than their substrates. Thus at least some of the absorption through the CdTe films in the following sets of measurements can be attributed to the LDS films.

The transmission measurements of sample G007 coupled with the CdTe film are shown in Fig 42 below.

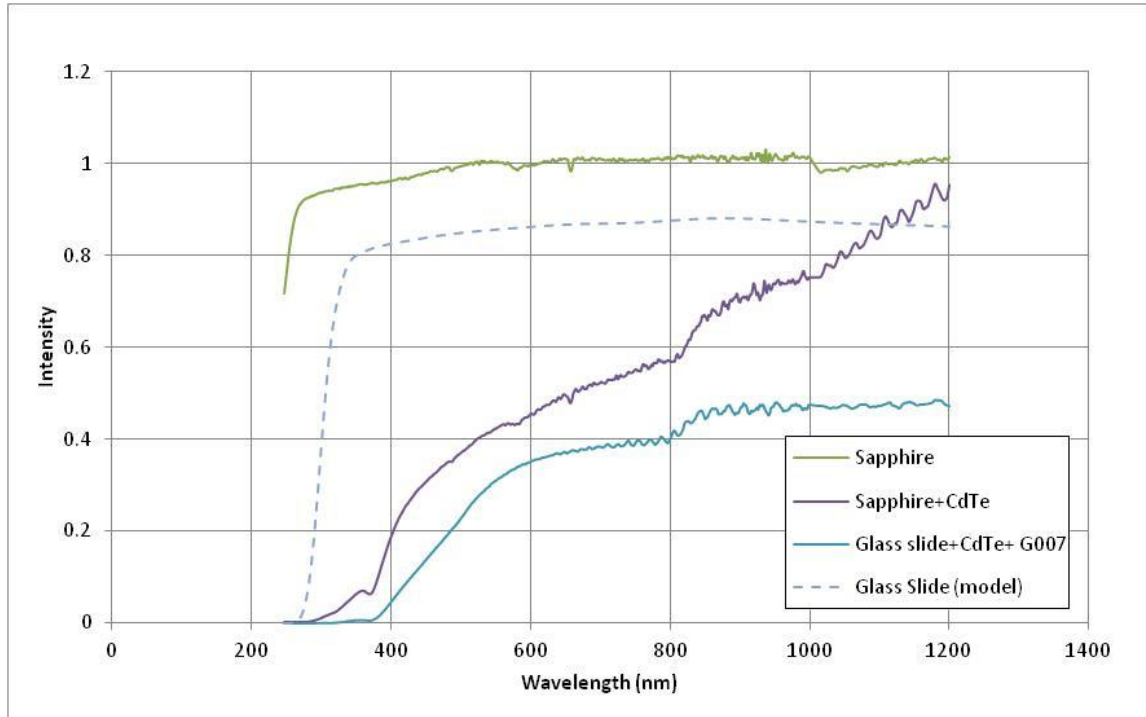


Figure 42: Results of transmission measurements of sample G007, compared to blank CdTe and the blank glass slide substrate

There is a significant decrease in transmission through the system compared to the blank glass substrate, suggesting a significant amount of absorption especially at shorter wavelengths. The blank CdTe film with no LDS layer exhibits higher transmission intensity than the sample with the LDS layer mounted on it. Although this is promising, as it suggests that there is more absorption with the application of the LDS layer, much of the absorption is likely due to the substrate rather than the film, as discussed previously.

Transmission measurements for sample CeORSO28 on CdTe are shown below.

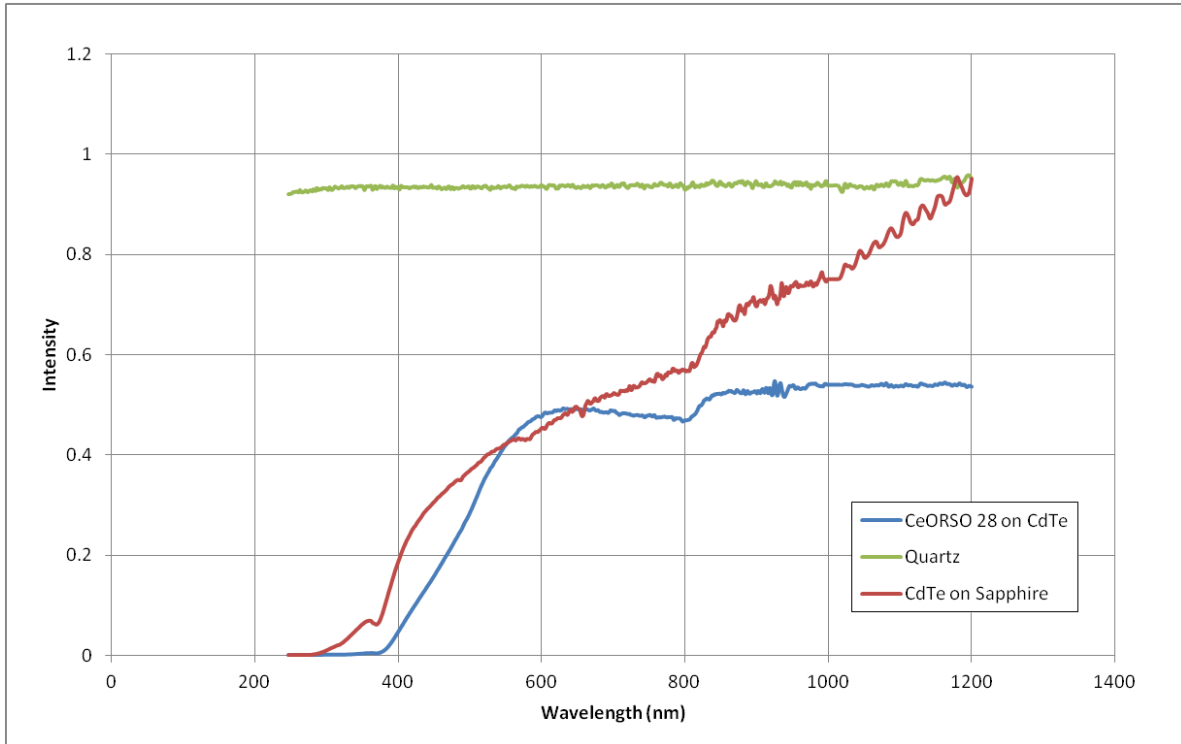


Figure 43: Results of transmission measurements of sample CeORSO-28, compared to blank CdTe and the blank quartz substrate

The transmission intensity through sample CeORSO28 on CdTe is much lower than the blank substrate (quartz) and the CdTe film with no LDS layer on it, suggesting that absorption was indeed occurring in the film. However, compared to the CdTe film with no LDS layer, there was also significantly lower transmission at long wavelengths. Since the corresponding absorption curve (Fig. 40) does not show an increase in absorption at these wavelengths, it is unclear why there is much lower transmission when there is no clear absorption mechanism at long wavelengths.

Transmission results for sample CeORSO27 mounted on a CdTe film are shown below.

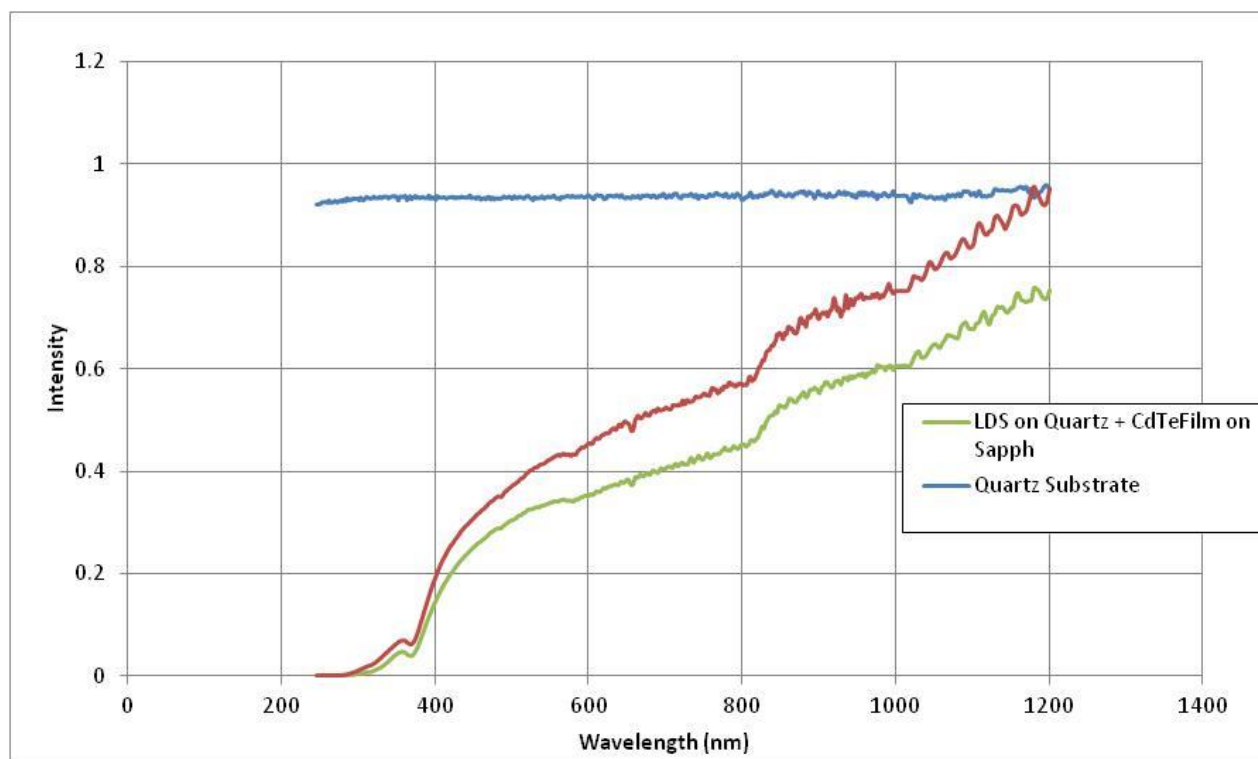


Figure 44: Results of transmission measurements of sample CeRORS-27, compared to blank CdTe and the blank quartz slide substrate

Despite exhibiting the strongest absorption of the three samples (Figs. 37 & 41) there was only a small decrease in the transmission at short wavelengths compared to the CdTe film with no LDS layer. However, both films exhibited significantly lower transmission (suggesting some absorption) than the blank quartz substrate. The discrepancy could be attributed to the ‘stacking’ process used in this measurement as opposed to the mounting process used for samples G007 and CeORSO28, which could have introduced more interface reflection effects that skewed results.

Overall, absorption spectroscopy and transmission ellipsometry measurements suggest that the LDS films contribute to stronger absorption at short wavelengths when coupled with CdTe films, as intended. With an ideal LDS film, optimized for quantum yield, the absorption in the 500-700nm range would also have increased due to the photoluminescence of the LDS film

in that range. Before testing with a fully optimized CdTe cell, another interesting experiment would be to test the LDS films in a similar structure with CdS films instead of CdTe. Since the goal is to shift incident light from short wavelengths to longer ones where they are not absorbed by the CdS window layer, absorption measurements would reveal the impact of this wavelength shift.

## VII. Conclusions

### a) Summary of Research Project

This research project investigated the use of cerium and terbium co-doped oxygen rich silicon oxide films as luminescent downshifting layers for cadmium telluride photovoltaic applications. A literature review showed that the high EQE region of CdTe fell between 500-700nm and thus many short wavelengths, high energy photons are unable to be efficiently utilized by the cell. The addition of a layer atop the solar cell that absorbed these ‘wasted’ photons and re-emitted them at more efficiently absorbed wavelengths was shown to improve the efficiency of the cell. Past experiments by members of the research group demonstrated that rare earth ion complexes coupled with silicon nano-structures could be made to emit very intensely around 550nm, making them a viable choice for downshifting layers for CdTe solar cells. This luminescence was found to be the result of an energy transfer process between cerium disilicate nanocrystals and terbium ions.

The goal of this project was to grow and characterize these rare earth doped layers to assess their suitability as luminescent downshifters. The samples were grown on silicon, quartz and glass slide substrates, using plasma enhanced chemical vapour deposition techniques. During growths, oxygen and silane flows were kept constant so that the atomic % of oxygen and silicon in the samples would remain constant at approximately 66% and 33% respectively. The temperature of the rare earth cells was increased to incorporate incrementally more cerium and terbium into the samples with each growth. Two samples, grown by former group member Patrick Wilson were also included in this research project. After deposition, the samples were cleaved and annealed in a quartz tube furnace at 1200°C for 60, 120, 240 and 480 minutes, to study the effect of annealing time on the optical properties of the films.

Rutherford Backscattering Spectrometry was used to determine the composition of the samples. While silicon and oxygen content were as expected, rare earth concentrations were several orders of magnitude lower than expected and did not display a clear correlation with cell temperature. This suggests that the lines or rings in the deposition system were likely clogged leading to low rare earth incorporation in the films.

Photoluminescence measurements confirmed a trend of increasing intensity with rare earth concentration and annealing time. At higher concentrations (upwards of 0.1 at. %) distinct cerium and terbium peaks were clearly visible, centred at 400 and 550nm respectively, confirming the rare earth energy transfer process. The wavelength of emission confirms that these films are potentially a good choice for luminescent downshifting applications for CdTe as peak emission intensity is within the high efficiency range of the solar cell. Ellipsometry measurements revealed a trend of increasing refractive index with annealing time, suggesting the formation of more nano-crystalline structures at longer anneal times. Also, some samples revealed the formation of additional intermediate layers with different optical properties between the substrate and the main layer.

UV-Visible wavelength absorption spectroscopy was performed on samples grown on glass slides and quartz substrates. Samples with higher rare earth concentration demonstrated strong absorption at short wavelengths and much lower absorption at  $\lambda > 400\text{nm}$ . The high absorption wavelengths correspond to the low EQE regions of the CdTe solar cells, which suggests that rare earth based LDS layers would exhibit minimal parasitic absorption at high EQE wavelengths. Transmission ellipsometry measurements revealed complementary results- samples with high rare earth concentrations exhibited low transmission at  $\lambda < 400\text{ nm}$  and significantly higher transmission at longer wavelengths. Pulsed Laser Deposition was used to grow thin film CdTe in

order to measure its optical response when coupled with LDS layers. Transmission ellipsometry measurements confirmed that when coupled with LDS films, CdTe exhibited stronger absorption at short wavelengths.

## **b) Improvements to Experimental Procedures**

There are several key improvements that could have been made to this research project. Primarily, when it became clear during initial sample growths that rare earth concentrations were much lower than expected, the cerium and terbium cell lines and rings should have been heated to sufficiently high temperatures to clear any blockages. This would also have addressed the issue of re-condensation of the rare earth carrier gases when passing through the cooler regions of the deposition system. In future experiments, RBS measurements should be performed early on, and then repeated periodically as samples are grown so as to confirm that growth parameters are actually resulting in the expected sample composition. A thorough calibration process should be performed before attempting to grow LDS samples.

Additionally, care should be taken to ensure that the furnace temperature remains constant throughout the annealing process. For several of the annealed samples, the furnace temperature dropped as low as 1090°C (for approximately 15-20 minutes which is relatively short in comparison to the longer anneal times of 480 minutes) early on in the annealing process, which could have resulted in changes in the formation of cerium disilicate nanostructures. This should be addressed by ramping up the furnace temperature in smaller increments and ensuring that the temperature is stable before placing the samples inside the tube. Ideally, a procedure should be developed to ensure that the sample transfer is rapid and efficient and to minimize the heat lost during the process.

Finally, during absorption and transmission measurements samples should be mounted onto CdTe films using optical glue where possible, instead of mechanically stacking them. This could reduce interface reflection effects and prevent mechanical damage by limiting delaminating of the films from the substrates due to scratching against one another. While delamination did not occur during these experiments, the samples had to be handled with extra care to ensure that there was no mechanical damage, which limited how, and how many experiments could be done.

### **c) Suggestions for Future Work**

In addition to implementing the changes suggested above, there are several key aspects to focus on for future experiments. Primarily, future growths should focus on incorporating a higher concentration of rare earth atoms into the LDS films, for a maximum of 10% Ce and 5% Tb, and the resulting optical and photoluminescence properties should be characterized.

Absorption and transmission measurements should also be repeated with CdS layers. While it was important to understand the effect of LDS on CdTe absorption, the goal of downshifting is to “bypass” absorption in the CdS layer, where the absorbed photons cannot be used to generate electron hole pairs. Thus, coupling the LDS layers with CdS films should minimize its absorption at short wavelengths, in order to ensure that more light is passing through to the CdTe region of the cell.

Since the results of this research project suggest that rare-earth based LDS films are a promising choice for CdTe photovoltaics, the next steps should be to perform quantum efficiency measurements to determine if they are a practical choice. Modelling or other analysis should initially be used to determine the minimum efficiency required to demonstrate an efficiency

increase in a CdTe solar cell, as well as to maintain or reduce the cost/kW for commercial applications.

The final step in characterizing the LDS layers should be to test them with a fully optimized CdTe solar cell to confirm the effect of the downshifting effect. However, due to the low sublimation temperature of CdTe (~600°C) and the high annealing temperature required by the LDS films (1200°C), traditional growth processes cannot be used. One possibility is to grow and anneal the LDS film on a transparent sapphire substrate, traditionally used for CdTe solar cells. After the LDS layer is grown and tested, it could be masked (or otherwise protected) and the solar cell grown on the ‘backside’ of the substrate, thus ensuring that the cell is not damaged by the high temperature treatment of the LDS films.

#### **d) Concluding Remarks**

As the demand for energy continues to grow at unprecedented rates, innovative solutions that provide a sustainable energy source while limiting environmental impact will play a key role in global development. Solar energy is a clean and abundant energy source and third generation photovoltaics are continuing to increase efficiencies and reduce costs. While single junction silicon solar cell technology is rapidly approaching its efficiency limits, CdTe photovoltaic technology still has the potential to vastly improve. Optical advances such as luminescent downshifting that lead to better absorption and current yields will likely advance this initiative.

This research project in conjunction with past work in the field, shows that rare earth based luminescent films are a promising material system for this application, due to ideal emission wavelengths, wide separation between the absorption and emission bands (leading to lower parasitic absorption) and ability to be grown using CVD techniques on a wide range of

substrates. However before this material system is ready for large scale applications, significant improvements need to be made in their quantum efficiency and growth processes. While this project unfortunately did not yield a functional LDS layer, the characterization of this material system could serve as the basis for the development of such a layer in the foreseeable future.

## VIII. Appendices

### Appendix A: Operation of MAC ECR PECVD system

#### From “weekend mode”

- 1) Check if nitrogen needs refilling → bar should be at or above mid level. If it does, refill nitrogen before starting.
- 2) If not, turn on nitrogen dewar (large grey tap-like valve), and switch on box. Both red lights should come on.
- 3) Wait for 15-20 minutes for cold-trap to refill (one of the red lights will turn off).
- 4) In the meantime, carry out safety checks
  - a. Check water valves are on at the back
  - b. Check silane flow.
  - c. Make sure pressures on gauges are right, against binder in the office.
  - d. On Panel 1
    - i. Return to main screen
    - ii. Instrument set up [5] → Verify column 2
    - iii. Gas selection [2] → verify GCF
    - iv. Zero Adjust [4] → highlight EXEC and use up and down arrows to zero
    - v. Baratron:
      1. Electrical: Pressure set up [7] → verify range is 100 mTorr → highlight EXEC, use arrows → DONE
      2. Zero mechanical baratron with small screwdriver.
- 5) Open diffusion pump valve (poppet valve)
  - a. Open manually using silver knob (beside nitrogen switch box)
  - b. Open pneumatic valve on Panel 2 (poppet valve)
- 6) Ensure main gate is closed.

#### Unloading sample from chamber

- 1) If there is a sample already inside the chamber:
  - a. Ensure that fork is pulled all the way back.
  - b. Open main gate, turn on chamber lamp
  - c. Insert fork into chamber and insert along grooves of sample holder

- d. Lower stage until holder separates from pegs and retract fork all the way.
- 2) Close main gate once fork is fully retracted.
- 3) Vent loadlock
  - a. Switch off IG1loadlock on Panel 1
  - b. Close Turbo gate on Panel 2
  - c. Open green nitrogen valve until loadlock pressure rises to atmosphere ( $7.6 \times 10^2$ )
- 4) Open black chamber door, and remove sample holder from fork, and ensure that you do not close chamber door all the way while nitrogen valve is open.

### **Loading sample into chamber**

- 1) Mount sample onto sample holder using metals clips, ensure it is not loose or falling out.
- 2) Blow off any dirt or debris using nitrogen gun.
- 3) Load sample back onto fork, making sure it's not jammed (i.e. it comes off easily)
- 4) Close chamber door, turn off nitrogen.
- 5) Close TP backing pump on panel 2.
- 6) Pump down loadlock:
  - a. Lean against black chamber door and open roughing valve (yellow tap like valve)
  - b. Keep opening valve slowly, watch pressure drop on loadlock, until at least  $5 \times 10^{-3}$ .
  - c. Close roughing valve.
- 7) Open TP backing, wait 10 seconds and open Turbo gate.
- 8) Turn on IG Chamber on Panel 1, wait for Loadlock pressure to reach Chamber pressure (~20 minutes)
  - a. IG loadlock should be at least  $10^{-6}$ .
- 9) Open Main gate on panel 2
- 10) Insert fork into chamber, align with sample stage
  - a. Raise/lower stage as needed until spokes are aligned with sample holder.
  - b. Retract fork all the way out of the chamber.
- 11) Close main gate.
- 12) Raise/lower stage as necessary.

### **Setting up heaters and power supplies**

- 1) Press "run" button on heater, wait for temperature to rise to 100C (~20 minutes)

- 2) Turn on Microwave power supply and magnet power supplies by turning on white and black switches on Panel 2.
  - a. Turn up temperature and current right before starting deposition
  - b. Make sure water supplies are on.

Setting up gas flows and rare earth deposition:

### **Gas Flows:**

- 1) Switch of IG Chamber on Panel 1
- 2) Select “Extended Display” on Menu
  - a. Change set points as necessary and select “on” for required gas flows
  - b. Turn on switches corresponding to required gas flows right before deposition.

### **Rare Earth Cells**

- 1) Cells should be heated up to 100C the night before.
- 2) Remember to turn on heater at the back to prevent lines from clogging
- 3) Lines and ring should be heated up, when starting up deposition (i.e. before loading sample)
- 4) Turn up cells to required deposition temperature.
  - a. Remember that RE argon flow lines have to be manually turned on using tap valves. Use thermal gloves!
  - b. Do this before opening RE switch on panel 1.

### **Starting deposition**

- 1) Turn on all required gas flows
  - a. Record partial pressure changes for each switch turned on\
- 2) Turn on stage rotation
- 3) Turn up magnet currents to 180A and 115A correspondingly, let them stabilize for ~10 minutes
- 4) Turn HV on, and turn knob so that Incident power- Reflected power = ~500W
  - a. Chamber should glow purple
- 5) When you’re ready to start the deposition, pull away shutter and start timer.

- 6) Close window shutter and place microwave shutter over window.

### **Stopping deposition**

- 1) Take off microwave shutter and open window shutter
- 2) Once required time is up, insert shutter back in, using black knob.
- 3) Turn of HV and re-zero knob
- 4) Turn down current knobs to zero.
- 5) Turn off heater by holding down “Run” button until it goes to zero (cool down should take ~1 hour)
- 6) Turn off gas flows on Panel 1
  - a. When turning of RE flows, remember to manually close valves for argon flow first
  - b. Turn off switches on panel

### **If running another deposition:**

- 1) Turn down RE cell temperatures to 100C (turn them up again closer to next deposition) but leave ring and line temperatures at 200C.

### **If not:**

- 1) Turn down all RE temperatures to 0C
- 2) Turn on fans to cool cells
- 3) Leave water running for at least 15minutes to cool off magnets

Follow steps to remove sample from chamber.

## IX. Works cited

- [1] U. E. I. Administration, "International Energy Outlook 2013," US Energy Information Administration, Nov 2013. [Online]. Available: <http://www.eia.gov/forecasts/ieo/world.cfm>.
- [2] Committee on America's Energy Future; National Academy of Sciences; National Academy of Engineering; National Research Council , America's Energy Future: Technology and transformation, Washington, DC: The National Academies Press, 2009.
- [3] Marian E. Koshland Integrated Natural Sciences Center, "Introduction to Semiconductors, Biography of an Experiment: The Invention of the Dye-sensitized Solar Cell," Haverford College, 2010. [Online]. Available: <http://www.haverford.edu/kinsc/boe/dssc/>. [Accessed 10 June 2014].
- [4] B. Streetman and S. Banerjee, Solid State Electronic Devices (6th Edition), Pearson Prentice Hall, 2006.
- [5] F. Meillaud, et. al., "Efficiency limits for single-junction and tandem solar cells," *Solar Energy Materials and Solar Cells*, no. 18-19, pp. 2952-2959, 2006.
- [6] W. Shockley and H. J. Queisser, "Detailed Balance Limit of Efficiency of p-n Junction Solar Cells," *Journal of Applied Physics*, vol. 510, no. 32, 1961.
- [7] Solar journey USA, "How Solar Works," Solar journey USA, 2009. [Online]. Available: <http://solarjourneyusa.com/bandgaps.php>. [Accessed 18 May 2014].
- [8] US Energy Information Administration, "Annual Energy Outlook 2013: Levelized Cost of New Generation Resources in the Annual Energy Outlook 2013," 2013. [Online]. Available: [http://www.eia.gov/forecasts/aeo/electricity\\_generation.cfm](http://www.eia.gov/forecasts/aeo/electricity_generation.cfm). [Accessed Feb 2014].
- [9] H. Schock, "Thin Film Photovoltaics," *Elsevier: Applied Surface Science*, vol. 96, pp. 606-616, 1996.
- [10] NREL, "Research cell efficiencies," NREL, 2013. [Online]. Available:

[http://www.nrel.gov/ncpv/images/efficiency\\_chart.jpg](http://www.nrel.gov/ncpv/images/efficiency_chart.jpg). [Accessed Feb 2014].

- [11] A. Shah, P. Torres, et. al., "Photovoltaic Technology: The Case for Thin-Film Solar Cells," *Science*, vol. 30, no. 5428, pp. 692-698, 1999.
- [12] B. E. McCandless and J. R. Sites, "Ch 14: CdTe Solar cells," in *Handbook of Photovoltaic Science and Engineering*, Chichester, J. Wiley & sons, 2003, p. 617.
- [13] e. a. D.H. Rose, "Technology Support for High-Throughput Processing of Thin-Film CdTe PV Modules: Phase 1 Annual Technical report," NREL, Golden, Colorado, 1999.
- [14] U. DOE, "SunShot Initiative: Cadmium Telluride," US Dept. of Energy, May 2013. [Online]. Available: [http://www1.eere.energy.gov/solar/sunshot/pv\\_cdte.html](http://www1.eere.energy.gov/solar/sunshot/pv_cdte.html). [Accessed Sept 2013].
- [15] P. Insider, "New record: First Solar hits 18.7% CdTe PV solar cell conversion rate - See more at: <http://news.pv-insider.com/thin-film-pv/new-record-first-solar-hits-187-cdte-pv-solar-cell-conversion-rate#sthash.2NPejnBA.dpuf>," PV Insider, March 2013. [Online]. Available: <http://news.pv-insider.com/thin-film-pv/new-record-first-solar-hits-187-cdte-pv-solar-cell-conversion-rate>. [Accessed 20 Sept 2013].
- [16] e. a. Lukas Kranz, "Doping of polycrystalline CdTe for high-efficiency solar cells on flexible metal foil," *Nature Communications*, vol. Article number: 2306, no. 4, 2013.
- [17] X. e. a. Wu, "16.5%-efficient CdS/CdTe polycrystalline thin-film solar cell," in *Conference Records 17th European Photovoltaic Solar Energy Conversion*, , Munich, 2001.
- [18] e. a. C. Strumpel, "Modifying the solar spectrum to enhance silicon solar cell efficiency: An overview of available materials," *Solar Energy Materials & Solar Cells*, vol. 91, pp. 238-249, 2006.
- [19] Optics.org, "DOE offers \$12M to break solar limit," Optics.org: The Business of Photonics, Jan 2013. [Online]. Available: <http://optics.org/news/4/1/39>. [Accessed Sept 2013].
- [20] P. Duxbury, "Theoretical and Practical limits on solar energy conversion : Why use nanostructuredmaterials?," Dept. of Physics, Michigan State University, Michigan, 2010.

- [21] E. K. e. al, "Enhancing the performance of solar cells via luminescent down-shifting of the incident spectrum: A review," *Science Direct: Solar EnergyMaterials&SolarCells*, vol. 93, pp. 1182-1194, 2009.
- [22] A. M. G. e. al, "Modeling Down-Conversion and Down-Shifting for Photovoltaic Applications," IEEE, Ottawa, ON, 2011.
- [23] K. R. M. B. S. Richards, "Overcoming the Poor Short Wavelength Spectral Response of CdS/CdTe Photovoltaic Modules via Luminescence Down-Shifting: Ray-Tracing Simulations," *PROGRESS IN PHOTOVOLTAICS: RESEARCH AND APPLICATIONS: Wiley Interscience*, vol. 15, pp. 27-34, 2007.
- [24] A. J. Kenyon, "Recent developments in rare-earth doped materials for optoelectronics," *Progress in Quantum Electronics*, vol. 26, pp. 225-284, 2002.
- [25] P. Wilson, "PhD Thesis: VISIBLE LIGHT EMISSION FROM SILICON-RICH SILICON NITRIDE AND CERIUM AND TERBIUM CO-DOPED SILICON OXIDE THIN FILMS," McMaster University, Hamilton, ON, 2012.
- [26] D. L. Dexter, "A Theory of Sensitized Luminescence in Solids," *The Journal of Chemical Physics*, vol. 21, pp. 836-850, 1953.
- [27] J. C. Bunzli and V. K. Pecharsky, "Handbook on the Physics and Chemistry of Rare Earths, Vol. 44," North Holland, Elsevier, 2013.
- [28] R. Dabkowski, "PhD Thesis: NEW ECR-PECVD REACTOR AND PRELIMINARY THIN FILM DEPOSITIONS," McMaster University, Hamilton, ON, 2011.
- [29] T. Thullier, "ELECTRON CYCLOTRON RESONANCE ION SOURCES," CERN Accelerator school, Geneva, 2012.
- [30] L. Gonchorova, "Rutherford Backscattering Spectrometry," University of Western Ontario, London, ON, 2013.
- [31] M. Mayer, "Workshop on Nuclear Data for Science and Technology: Materials Analysis,"

- International Atomic Energy Agency, UNESCO, 2003.
- [32] Evans Analytic Group, "Materials Characterization: RBS Theory -- Kinematics," Evans Analytic Group, 2010. [Online]. Available: <http://www.eag.com/mc/rbs-kinematics.html#next>. [Accessed February 2014].
- [33] M. Mayer, "SIMNRA Home Page," Max Plank Institut fur Plasmaphysik, 2011. [Online]. Available: <http://home.rzg.mpg.de/~mam/index.html>. [Accessed May 2014].
- [34] C. Smith, "Ellipsometry: School of Physics, Surface and Interface Physics," Trinity College Dublin, 2008. [Online]. Available: <https://www.tcd.ie/Physics/Surfaces/ellipsometry2.php>. [Accessed May 2014].
- [35] J.A. Woollam Co. Inc., "Complete Ease Data Analysis Manual, p 126," J.A. Woollam Co. Inc., Nebraska, 2011.
- [36] The Gruebele Group, "UV-visible molecular absorption spectroscopy," Center for Biophysics and Computational Biology, The University of Illinois at Urbana-Champaign, Illinois, 2009.
- [37] S. Jovanovic, "M.A.Sc. Thesis: Pulsed Laser Heteroepitaxy of High Quality CdTe Thin Films on Sapphire Substrates," McMaster University, Hamilton, ON, 2013.
- [38] R. Savidge, "Master's Thesis: Down-shifting of Light by Ion Implanted Samples for Photovoltaic Applications," McMaster University, Hamilton, ON, 2012.
- [39] B. J. a. C. Herzinger, "Quantifying the accuracy of ellipsometer systems," J.A. Woollam & Co., Lincoln, Nebraska, 2007.
- [40] e. a. Lilli Soovali, "Uncertainty sources in UV-Vis spectrophotometric measurement," Springer Verlag, Tartu, Estonia, 2006.
- [41] International Energy Agency, "A Snapshot of Global PV: 1992-2012," IEA PVPS, Switzerland, 2013.